ACS PHYSICAL CHEMISTRY Au
AN OPEN ACCESS JOURNAL OF THE AMERICAN CHEMICAL SOCIETY



pubs.acs.org/physchemau
Article

# Synergistic Niobium Doped Two-Dimensional Zirconium Diselenide: An Efficient Electrocatalyst for $O_2$ Reduction Reaction

Ashok Singh and Srimanta Pakhira*

Cite This: ACS Phys. Chem Au 2024, 4, 40−56
Read Online

ACCESS | Metrics & More | Article Recommendations | Supporting Information

**ABSTRACT:** The development of high-activity and low-price cathodic catalysts to facilitate the electrochemically sluggish $O_2$ reduction reaction (ORR) is very important to achieve the commercial application of fuel cells. Here, we have investigated the electrocatalytic activity of the two-dimensional single-layer Nb-doped zirconium diselenide (2D Nb-$ZrSe_2$) toward ORR by employing the dispersion corrected density functional theory (DFT-D) method. Through our study, we computed structural properties, electronic properties, and energetics of the 2D Nb-$ZrSe_2$ and ORR intermediates to analyze the electrocatalytic performance of 2D Nb-$ZrSe_2$. The electronic property calculations depict that the 2D monolayer $ZrSe_2$ has a large band gap of 1.48 eV, which is not favorable for the ORR mechanism. After the doping of Nb, the electronic band gap vanishes, and 2D Nb-$ZrSe_2$ acts as a conductor. We studied both the dissociative and the associative pathways through which the ORR can proceed to reduce the oxygen molecule ($O_2$). Our results show that the more favorable path for $O_2$ reduction on the surface of the 2D Nb-$ZrSe_2$ is the $4e^-$ associative path. The detailed ORR mechanisms (both associated and dissociative) have been explored by computing the changes in Gibbs free energy ($\Delta G$). All of the ORR reaction intermediate steps are thermodynamically stable and energetically favorable. The free energy profile for the associative path shows the downhill behavior of the free energy vs the reaction steps, suggesting that all ORR intermediate structures are catalytically active for the $4e^-$ associative path and a high $4e^-$ reduction pathway selectivity. Therefore, 2D Nb-$ZrSe_2$ is a promising catalyst for the ORR, which can be used as an alternative ORR catalyst compared to expensive platinum (Pt).

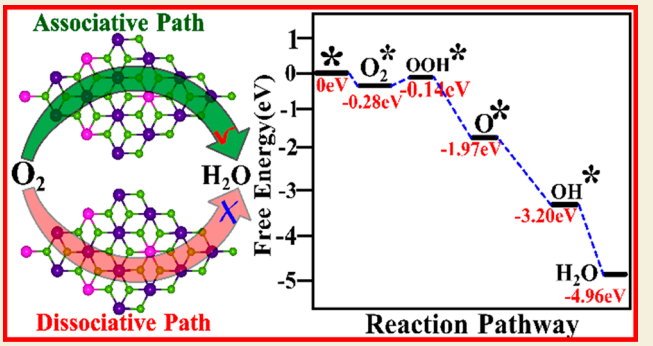


**KEYWORDS:** *$O_2$ reduction reaction, two-dimensional transition metal dichalcogenides (2D TMDs), electronic structure, associative and dissociative mechanism, adsorption energy, Gibbs free energy, electrocatalytic activity*

## INTRODUCTION

The escalating global population and ongoing advancements in global industrialization and society have led to a significant surge in global energy demand. Nowadays, a great part of the energy demand over the world is fulfilled by fossil fuels.[1] However, the bitter truth is that the traditional resources of fossil fuels are in danger of being depleted with indefinite extraction and utilization.[1] In addition to this, the consumption of fossil fuels results in the emission of pollutants. So, the concern about the energy crisis, environmental pollution, and climate change have put at risk the future of human society.[2] The gradual exhaustion of fossil fuels and the detrimental impact on the environment caused by pollution have provoked scientists and researchers all over the world to develop renewable, sustainable, eco-friendly, and highly efficient energy resources.[3]

Renewable energy systems, including fuel cells and metal−air batteries, are efficient solutions to reduce environmental issues and alleviate energy demand. These technologies are primarily realized in the water cycle. The fuel cell has gained significant attention among alternatives to fossil fuels due to its impressive conversion efficiency, reliable performance, fast startup, operation at low temperatures, and minimal emissions. The fuel cell converts chemical energy directly to electricity without the emission of pollutants. In other words, Hydrogen ($H_2$), which is generated by harvesting sustainable solar and wind energies, is used as input and results in power generation with absolutely zero emission.[4] So, fuel cells are the ideal choice for energy conversion and power sources for a healthy and sustainable future. The fuel cell relies on some of the electrochemical reactions, such as hydrogen evolution reaction (HER), ORR, and oxygen evolution reaction (OER). However, the practical growth of fuel cells has been extensively

Received: July 22, 2023
Revised: October 3, 2023
Accepted: October 3, 2023
Published: October 25, 2023

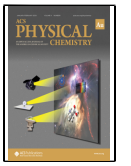

hindered by the inherent thermodynamic limitation of the ORR.[5] To utilize the ideal performance of the fuel cell, it is necessary to hasten the kinetics of the ORR. So, today's demand is to develop an active material that can serve as an efficient catalyst and would assist to accelerate the kinetics of the cathodic reaction.

To date, platinum (Pt) and Pt-based materials serve as a suitable catalyst for the reduction of $O_2$ at the cathode in the fuel cell.[6−8] Moreover, a sizable overpotential higher than 0.20 V is observed, even with the state-of-art Pt-based catalyst.[9] The utilization of Pt catalysts account for approximately 40−50% of the total cost associated with fuel cell stacks.[10] So, the cost of the fuel cell imposes serious limitations on the commercialization of the fuel cell. Moreover, the shortage of noble metals in the earth's crust and their insufficient stability toward the byproducts hinder their widespread applications in modern science and technology. Thus, the mass production of such types of electrocatalysts is not feasible. Mainly the mass production of the ORR catalysts is impeded by the following three limitations: (1) the high cost,[10] currently, the Pt has been recognized as an effective catalyst in the fuel cells, which has a limited reserve and has resulted from the high cost of the fuel cells, and (2) the low performance,[11] another factor is the deficiency of the active sites on the catalyst. To actively use the efficiency of the fuel cells, it is necessary to fabricate a catalyst with a large number of active sites and specific selectivity, and (3) poor stability[12] is another factor, which is the cause of the degradation of fuel cell performance, and is the stability of the catalysts toward the byproducts formed during the operation of the fuel cell. The quest for enhanced catalysts for the ORR has sparked advancements in the identification of nonprecious metal-based catalysts that exhibit superior catalytic activity compared to Pt.

In this pursuit, researchers have explored various metals both in their pure state and through the process of alloying with other metals. Pt, Pd, Au, Ag, and Ni clusters are to be effective to catalyze oxygen reduction in their pure form.[13] Wang et al. have extensively documented the efficacy of synergistic Mn−Co catalysts in facilitating high-rate ORR.[14] Numerous recent studies have provided substantial evidence to support the exceptional catalytic properties of metal oxides and sulfides in the context of ORR, which gives efficiency as good as the state of art Pt/C catalyst.[15,16] Although metal catalysts have demonstrated excellent catalytic activity, considering the low availability of metal in the earth's crust and huge cost, the expansion of a cheap and efficient catalyst is a paramount need for realizing the practical applications of fuel cells.

As a typical earth-abundant material, transition-metal compounds, such as transition metal oxides, metal chalcogenides, metal phosphides, metal carbides, metal nitrides, etc. have been widely used as promising catalysts for electrochemical mechanisms in fuel cells and energy conversion applications.[17] Among all of the transition metal compounds, two-dimensional transition metal dichalcogenides (2D TMDs) have gained significant interest as catalysts for electrochemical reactions. The unique properties of 2D TMDs which make them suitable for the catalyst are (1) large surface area: the 2D TMDs have a high surface-to-volume ratio which provides a large density of active sites; (2) stability and thermal conductivity: as the 2D TMDs have only planar covalent bonding, they show excellent mechanical strength and remarkable resilience, and thermal conductivity enables efficient dispersion of heat generated during exothermic reactions; (3) tunable electronic properties: the electronic properties of the 2D TMDs materials can be tailored by creating defects, doping, stress, etc.[18] The electronic properties, in turn, tailor the catalytic performance of the materials. Owing to the above properties, the 2D TMDs are good candidates for the electrocatalyst of electrochemical reactions.

In the wide family of the 2D TMDs, 2D $MoS_2$ has emerged as a highly investigated material due to its remarkable catalytic capabilities.[19] $MoS_2$ has been considered a promising non-noble HER catalyst but only the edge site shows high HER activity.[20,21] In other words, experimental and computational studies confirm that the electrocatalyst activity of the $MX_2$ (where M is transition metal atoms and X is chalcogens) is closely correlated with the edge side while the basal plane with a large area is generally inactive.[22,23] To the best of our knowledge, optimization of both active site and electronic properties of the 2D $MX_2$ electrocatalysis is highly required. As we know the basal plane of the 2D TMDs constitutes a large surface area, therefore if the inert basal planes could be activated, high electrocatalytic activity would be expected. To activate the inert basal plane and tailor the electronic properties, various strategies have been developed such as creating defects,[24,25] metal doping,[26,27] nonmetal substitution, strain engineering,[28] phase engineering, etc.[29]

Among all the strategies, substitutional doping is considered a suitable technique, as it provides long-term stability without degrading performance. The dopant atoms change the spin-density distribution around them, which would change the strength of $O_2$ adsorption and other reaction species. So, the ORR process can be performed on the surface of the 2D TMDs near the appropriate doping atoms. For instance, Xiao et al. theoretically demonstrated the favorable catalytic activity of the Co/Ni-doped 2D $MoS_2$ toward ORR.[30] Pumera et al. put forward the idea that introducing Fe and Mn dopants into the 2D $MoS_2$ can promote its catalytic activity in the context of ORR.[31] Recently, Upadhyay and Pakhira computationally analyzed that the 2D monolayer Pt-doped $MoSe_2$ exhibits a superior catalytic activity toward ORR.[27] Moreover, the doping of $MoS_2$ by heteroatoms such as P and N exhibits moderate adsorption strength of oxygen molecules and enhances the ORR.[32,33] In a recent study by Tain and Tang, it was discovered that the addition of Ni or Co to materials such as 1T-$TiS_2$, 2H-$TiS_2$, 1T-$ZrS_2$, 1T-$NbS_2$, and 2H-$TaS_2$ results in a promising electrocatalytic activity for the ORR. The overpotential required for ORR on these doped materials was found to be within the range of 0.32−0.55 V, which is comparable to that of the most advanced electrocatalysts currently available (i.e., Pt).[34] It has been shown that the 2D monolayer $ZrSe_2$ is a new material of TMDs, has been successfully prepared experimentally, and has 1T phase as a stable structure.[35−37] Moreover, earlier predictions show that at low vacancy density, the $ZrSe_2$ and $ZrTe_2$ TMDs have a low value of hydrogen adsorption energy ($\Delta E^{H}$) and the value of $\Delta G$ is very close to that of Pt.[38]

In a recent theoretical study, Som and Jha showed an important observation regarding the catalytic activity of both the 2D single layer $ZrS_2$ and $ZrSe_2$ materials. They found that the edge sites of these materials, rather than the basal planes, play a crucial role in accelerating the HER. To further enhance the HER kinetics, the researchers decided to introduce the Nb, Pt, and W dopants in both the 2D $ZrS_2$ and $ZrSe_2$ materials. Interestingly, they discovered that the 2D Nb-doped systems, namely, Nb-$ZrS_2$ and Nb-$ZrSe_2$, exhibited a robust metallic


https://doi.org/10.1021/acsphyschemau.3c00035
ACS Phys. Chem Au 2024, 4, 40−56

nature, which significantly boosted their catalytic activity toward HER. Furthermore, they observed that, on the basis of $\Delta G$ calculations, 2D monolayer Nb-$ZrSe_2$ has the best catalytic activity toward HER.[39] In addition, 2D $ZrSe_2$ possesses important characteristics that make it a favorable choice. It is nontoxic, affordable, and exhibits strong resistance to corrosion. Furthermore, it has been successfully synthesized on a large scale and experimented with in the form of thin atomic layers.[40] In the context of sulfur- and selenium-based $ZrS_2$ or $ZrSe_2$ TMDs, the presence of S or Se with a $2^-$ valence ($S^{2-}$ or $Se^{2-}$) enhances the reduction capacity, thereby promoting the activity of the ORR.

Motivated by the extensive research attention and extraordinary catalytic activity of the Nb-doped $ZrSe_2$ toward HER, it is the fundamental interest to explore the more catalytic applications of the 2D Nb-$ZrSe_2$ toward ORR. In this work, a DFT-D calculation is performed to explore the catalytic activity of the 2D monolayer Nb-$ZrSe_2$ toward ORR. In principle, we aimed to answer these questions: how the doping of Nb alters the structural and electronic properties of the 2D monolayer $ZrSe_2$? Do the 2D Nb-$ZrSe_2$ catalyst act as an efficient ORR catalyst? If yes, which path it will follow to reduce the $O_2$? To answer these questions, we have analyzed the structural and electronic properties of the 2D Nb-$ZrSe_2$ and examined the changes of Gibbs free energy ($\Delta G$) for all ORR intermediates at their minimum-energy condition. This study addresses some unique properties of 2D monolayer Nb-$ZrSe_2$ and suggests that it can act as an efficient and useful catalyst for the ORR mechanism. Thus, 2D Nb-$ZrSe_2$ can serve as an efficient cathodic catalyst in fuel cells and metal−air batteries.

## THEORY, METHODOLOGY, AND COMPUTATIONAL DETAILS

The ORR has an essential role in the functioning of fuel cells. These electrochemical devices are designed to convert the chemical energy of the fuel, typically $H_2$, directly into electrical energy. The working principle of the fuel cell can be defined as follows:[41,42] $H_2$ is produced by the electrocatalytic cell as fuel is brought into the anode side of the fuel cell. At the anode side, $H_2$ undergoes a reaction, resulting in the generation of electrons and protons:

$$H_2 \rightarrow 2H^+ + 2e^-$$

The protons ($H^+$) pass through the membrane, while the accompanying electrons travel through the electric circuit. They combine together at the cathode side of the fuel cell with oxygen. At the cathode, oxygen is reduced to water by reacting with $H^+$ and $e^-$ through the electrochemical reaction:[43,44]

$$2H^+ + \frac{1}{2}O_2 + 2e^- \rightarrow H_2O$$

All these processes rely on some electrochemical reactions. Among them, ORR is one of the reactions at the cathode that reduces the oxygen molecule to water.

ORR reaction involves oxygen diffusion, i.e., the $O_2$ adsorption on the surface of the catalysts followed by the $H^+ + e^-$ transfer processes to reduce the $O_2$ into water. The oxygen reduction in acidic media mainly occurs through two different pathways:[45,46] either a four-electron reduction pathway from $O_2$ to $H_2O$ or two electron pathway from $O_2$ to $H_2O_2$.

Direct $4e^-$ reduction:

$$O_2 + 4H^+ + 4e^- \rightarrow 2H_2O \quad E^o = 1.23\ \text{eV}$$

Indirect reduction:

$$O_2 + 2H^+ + 2e^- \rightarrow H_2O_2 \qquad E^o = 0.68\ \text{eV}$$

$$H_2O_2 + 2H^+ + 2e^- \rightarrow 2H_2O \quad E^o = 1.77\ \text{eV}$$

The indirect $2e^-$ pathway produces corrosive peroxide ($H_2O_2$) intermediates, which may corrode the catalytic surface; hence, there would be concern about the stability of the fuel cell. Moreover, the formation of $H_2O_2$ hinders the process and kinetics of the ORR reaction but also deteriorates the polymer membrane by generating reactive radicals. Thus, four electron pathway is preferred and considered more efficient than that of the two-electron pathway. Based on how the O═O bond breaks, the $4e^-$ pathway can be divided into two different reaction pathways:[47] (1) $O_2$ decomposition pathway: in this path the $O_2$ is adsorbed on the surface of catalyst and followed by the cleavage of $O_2$ bond. Then, it involves a series of electron−proton transfer reactions to reduce $O_2$ into water. The detailed reaction steps can be described as follows:

$$O_2 + * \rightarrow O_2^*$$

$$O_2^* \rightarrow 2O^*$$

(2) OOH dissociation path: the $O_2$* reacts with $H^+$ and $e^-$ coming from the anode side to form OOH*. Then, cleavage of the O═O bond occurs into O* and OH*. After that, the hydrogenation of the O* occurs to form the next OH*. Finally, the removal of $H_2O$ occurs on the surface of the catalyst. The details can be described as follows:

$$O_2^* + H^+ + e^- \rightarrow OOH^*$$

$$OOH^* \rightarrow O^* + OH^*$$

$$O^* + H^+ + e^- \rightarrow OH^*$$

$$OH^* + H^+ + e^- \rightarrow H_2O$$

Where the asterisk * denotes the adsorption site. In summary, we can say that the ORR reaction basically relies on the cleavage of O═O bond and protonation of the ORR intermediates.

The catalytic potential of the 2D Nb-$ZrSe_2$ toward ORR is measured combinedly by computing and analyzing the adsorption energy with the values of $\Delta G$ of each intermediate species during the subject reaction. We used computational hydrogen electrode (CHE) method to calculate the adsorption energy and the values of $\Delta G$ of each intermediate. In this method, the energies are calculated under the standard conditions (pH = 0, $p$ = 1 bar, $T$ = 298.15 K, and $U$ = 0 V). We have implemented the approach introduced by Nørskov et al. in our study. Their research showcased a significant finding that the chemical potential of $H^+ + e^-$ can be correlated with 1/2 $H_2$ in the gaseous state, which was determined using the standard hydrogen electrode.[9] Consequently, under the standard conditions, we can calculate the energy change of the reaction A + H → A + $H^+ + e^-$ by employing the reaction A + H → A + 1/2 $H_2$. The adsorption (or binding) energies ($\Delta E$) presented in this study has been calculated as the energy difference between the energy of the model with adsorbed species [$E_{slab+adsorbate}$] and the energy of


https://doi.org/10.1021/acsphyschemau.3c00035
ACS Phys. Chem Au 2024, 4, 40−56

the catalytic model [$E_{slab}$] and the energy of the adsorbate [$E_{adsorbate}$] according to the following equation:[48]

$$\Delta E = E_{slab+adsorbate} - E_{slab} - E_{adsorbate}$$

Negative adsorption energy indicates that the adsorbed oxygen intermediates are attached to the catalytic surface stably. In other words, a negative adsorption energy signifies that the adsorbate is likely to bind energetically to the catalyst surface, indicating a favorable interaction between them. Therefore, a negative adsorption energy is favorable for elementary reactions over the catalytic surface. The value of $\Delta G$ in each reaction step was evaluated as[49,50]

$$\Delta G = \Delta E + \Delta E_{ZPE} - T\Delta S$$

where $\Delta E$ denotes the adsorption energy obtained from the DFT-D calculations of the equilibrium structures and $\Delta E_{ZPE}$ and $\Delta S$ represent the change in zero-point energy and entropy correction, respectively. $T$ denotes room temperature 298.15 K in this calculation.

The overpotential, which is noted by $\eta$, is an important parameter that reflects the energy barrier for a given electrochemical reaction, such as ORR. The relationship $\eta = \Delta G_{max}/e^- + 1.23$ V is employed to calculate the overpotential[51] where $\Delta G$ is the maximum change in Gibbs free energy of elementary steps during the $O_2$ reduction reaction and 1.23 Vs SHE is the thermodynamic potential.

For all the systems studied here (i.e., $ZrSe_2$, Nb-$ZrSe_2$, and ORR intermediates), the equilibrium atomic configuration, structures, electronic properties, and energetics were obtained by using the spin-unrestricted B3LYP DFT framework implemented in CRYSTAL17 suite code.[52] The hybrid functional B3LYP provides reasonable accuracy in the band gap calculations. It has a much lower computational cost and is easier to converge. Additionally, the inclusion of Grimme's "-D3" dispersion correction further improves the performance of the hybrid functionals. To account the weak nonbonding van der Waals (vdW) interactions between the reactants or intermediates and the interface, we incorporated the damped vdW dispersion correction (-D3) within the framework of density functional theory (DFT), specifically known as DFT-D3.[53] Ying et al. reported in their review article that the B3LYP hybrid functional improves the energy gaps of a variety of materials from bulk to surface.[54] Muscat et al. established the reliability of the B3LYP hybrid functional to predict the band gap of a variety of materials using the local Gaussian basis set in CRYSTAL suit code or software.[55] They claimed that the B3LYP hybrid functional reproduced observed band gap reliably in a wide range of the materials, which are in good agreement with the experimental values and obtained from more sophisticated correlated calculations or perturbation theories.[55] By considering the advantages and reasonable accuracy, and the track record of the B3LYP hybrid functional in computational science, we employed the B3LYP hybrid functional. To utilize the hybrid functional, we used the "FMIXING" keyword to mix the FOCK/KS matrix, and we employed 80% FOCK/KS matrix mixing to maintain the accuracy of the calculations. A 2 × 2 supercell of the 2D monolayer structure of the pristine $ZrSe_2$ was considered and one Zr atom was substituted by one Nb atom to form the 2D monolayer Nb-$ZrSe_2$ structure, and all the ORR reaction steps on the surface of the 2D Nb-$ZrSe_2$ were investigated in the present study. We have utilized the Gaussian types of atomic basis sets to define the atomic orbitals, which have been found to yield more precise outcomes compared to plane wave basis sets.[56,57] In simpler terms, although the computational procedure differs from the plane wave code (i.e., VASP, Quantum Espresso), both approaches yield identical results. In the realm of hybrid density functionals, localized Gaussian basis set codes are inherently well-suited for addressing the Hartree−Fock (HF) component of the outcome.[58,59] For the Zr, Se, O, H, and Nb atoms, triple-$\zeta$ valence polarized (TZVP) Gaussian basis set were used in the present calculations.[60,61] We employed full optimization process, i.e., all atomic coordinates and lattice parameters were allowed to relax during geometry optimization. The convergence criterion for the self-consistent field (SCF) was established as a total energy difference of $10^{-7}$ a.u. between two consecutive iterations. The threshold controlling of the coulomb exchange integral calculation was controlled by the five-threshold set 7, 7, 7, 7 (ITOL1 to ITOL4), and 14 (ITOL5) for both the geometry optimization and electronic property calculations. The CRYSTAL17 code utilizes the default threshold for geometry optimization on all atoms, employing specific values for maximum and RMS force (0.000450 and 0.00300 au, respectively) and maximum and RMS displacement (0.001800 and 0.001200 au, respectively). To ensure accurate 2D monolayer, i.e., SLAB calculations using the CRYSTAL17 code, we have established a separation of 500 Å in the normal surface direction of the 2D monolayer Nb-$ZrSe_2$ along $Z$-direction where is no symmetry.[27,62] This distance effectively prevents any spurious interactions between the periodic images of the monolayer slab. Our current calculations indicate that this separation is sufficient to mitigate any undesired influences. While no computational tool is entirely exempt from limitations, we believe that our use of the CRYSTAL17 code is justified based on its track record. Numerous studies have been performed which provide a comprehensive overview of the CRYSTAL's capabilities, algorithms, and validation of the outcomes against experimental data and other benchmark data.[63−66] These studies provide insights into code reliability. Furthermore, various applications of this code in the fields of solid-state chemistry and physics, quantum mechanics, and catalysis have been done. In this work, to ensure that the code CRYSTAL accurately captured the properties under investigation, we rigorously validated our results by comparing them with available experimental data and complementary calculations from other well-established codes. To perform the integration within the Brillouin zone, we have used 16 × 16 × 1 k-mesh in the Monkhorst pack scheme[67] for the pristine 2D $ZrSe_2$, Nb-$ZrSe_2$, and all the reaction intermediates for both the geometry optimization and electronic property calculations. The electronic band structure was constructed along the high-symmetry $k$-path direction $\Gamma$-$M$-$K$-$\Gamma$ of the corresponding irreducible Brillouin zone. All the equilibrium structures with the images were plotted by using VESTA software.[68]

## RESULTS AND DISCUSSION

The equilibrium structure of the 2D monolayer $ZrSe_2$, which is the main object of this present work, belongs to the 1T phase (i.e., one atom of Zr is octahedrally coordinated by six atoms of Se) as shown in Figures 1 and 2. By using VESTA software, a 2D monolayer $ZrSe_2$ primitive cell was computationally designed, and a model system has been developed for further studies, and the structure was optimized by using the first principle-based periodic dispersion-correction hybrid DFT


https://doi.org/10.1021/acsphyschemau.3c00035
ACS Phys. Chem Au 2024, 4, 40−56

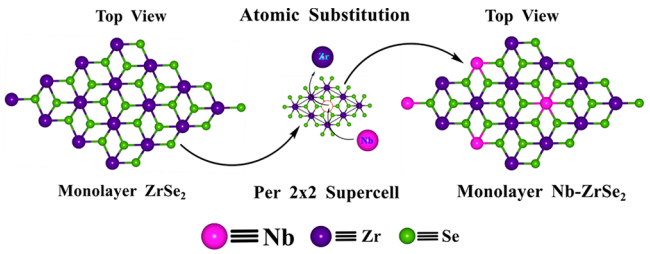


**Figure 1.** Representation of 2D monolayer $ZrSe_2$ and 2D monolayer Nb-$ZrSe_2$.

(DFT-D3, noted by B3LYP-D3) method as shown in Figure 1. The structure is a trigonal 2D slab system with $P\bar{3}m1$ layer group symmetry, and the computed unit cell parameters, i.e., the lattice constants are about $a = b = 3.75$ Å of the 2D pristine monolayer $ZrSe_2$ which is well consistent with the previously reported values.[39,40] Each unit cell consists of one Zr and one Se atom, as shown in Figures 1 and 2. Then, the doped system is constructed by substituting one Zr atom with one transition metal Nb per 2 × 2 supercell of the 2D monolayer pristine $ZrSe_2$ as illustrated in Figure 1. The doping was defined by the following equations:

$$\theta = \frac{\text{number of doping atoms per } 2 \times 2 \text{ supercell}}{\text{number of total metal atoms in } 2 \times 2 \text{ supercell}}$$

So, the Nb dopant atom amounts to 25% (only metal atom doping) atomic substitution per 2 × 2 supercell of the 2D $ZrSe_2$. The 2D monolayer 2 × 2 structure of the Nb-$ZrSe_2$ consists of one Nb, three Zr, and eight Se atoms per one unit cell as represented in Figure 2. The 2D Nb-$ZrSe_2$ system is then fully relaxed with respect to both atomic coordinates and cell parameters by the same level of the DFT-D method during optimization. The equilibrium lattice parameters of the 2D Nb-$ZrSe_2$ were found to be $a = b = 7.38$ Å as represented in Figure 2. All the fully relaxed geometrical data of the 2D monolayer $ZrSe_2$ and Nb-$ZrSe_2$ material have been reported in Table 1 and represented in Figure 2. The ORR mechanism involves the movements of the electrons; i.e., the transfer or transportation of electrons is a key process during the electrochemical ORR mechanism. Previous studies have shown that the electronic properties (i.e., electronic band gap, band structure, and total density of states) of catalysts have a significant impact on their catalytic efficiency. The electronic properties have been analyzed by computing and observing the electronic band structure and total density of states (DOSs) of both the 2D

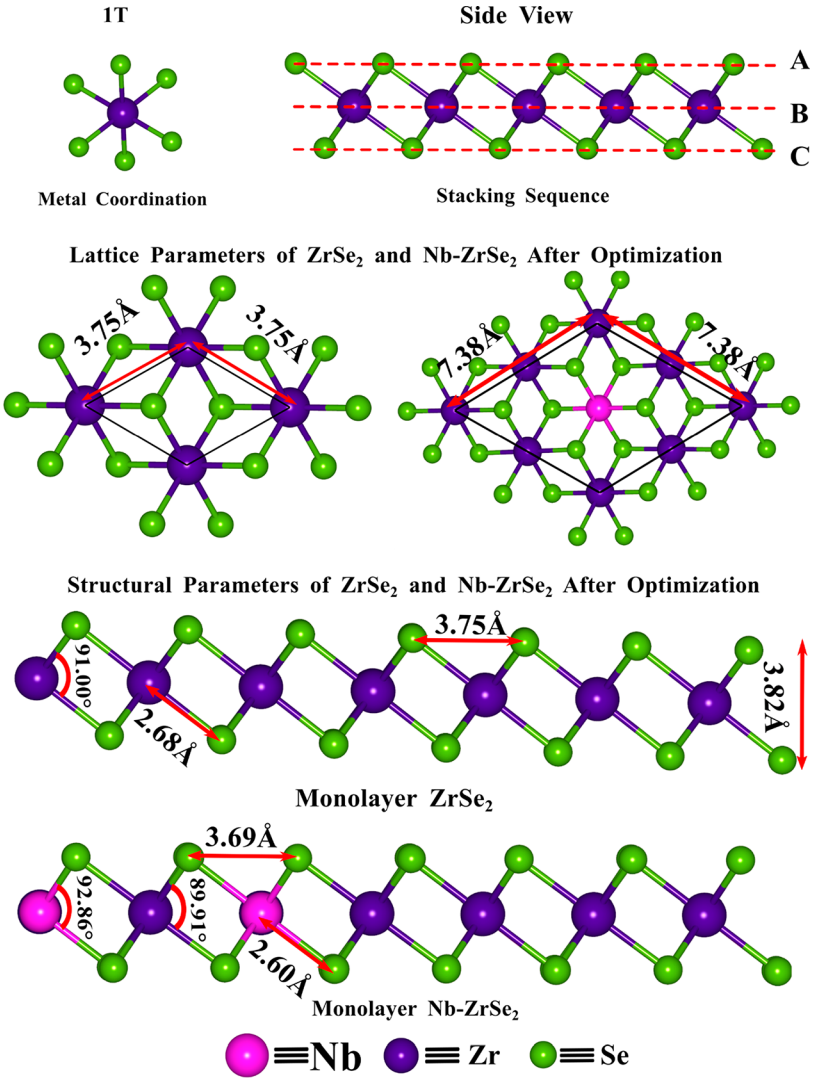


**Figure 2.** Metal coordination, stacking sequence, unit cell, and structural properties of $ZrSe_2$ and Nb-$ZrSe_2$.


https://doi.org/10.1021/acsphyschemau.3c00035
ACS Phys. Chem Au 2024, 4, 40−56

**Table 1. Equilibrium Structural Properties of the 2D Monolayer $ZrSe_2$, 2D Monolayer Nb-$ZrSe_2$, and Comparison with Previously Reported Data**

| System | Lattice parameters (Å) | Interfacial angle in degree | Layer group and symmetry | Average bond length Zr−Se (Å) | Average bond length Nb−Se (Å) | References |
|---|---|---|---|---|---|---|
| $ZrSe_2$ monolayer | $a = b = 3.75$ | $\alpha = \beta = 90°$ $\gamma = 120°$ | $P\bar{3}m1$ | 2.68 | - | This work |
| $ZrSe_2$ monolayer (previously reported) | $a = b = 3.77$ | $\alpha = \beta = 90°$ $\gamma = 120°$ | $P\bar{3}m1$ | 2.70 | - | 39, 40 |
| Nb-$ZrSe_2$ monolayer | $a = b = 7.38$ | $\alpha = \beta = 90°$ $\gamma = 120°$ | $P1$ | 2.67 | 2.60 | This work |

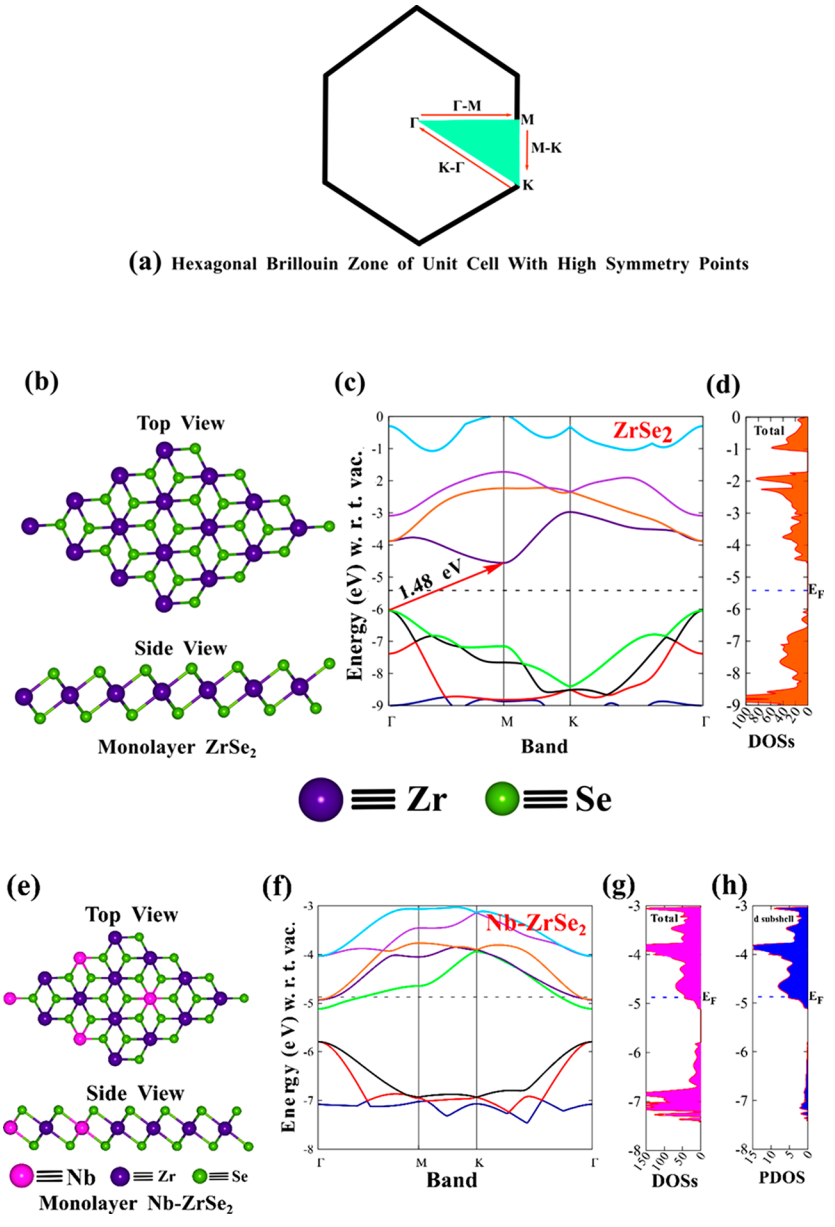


**Figure 3.** (a) Brillouin zone with high symmetry k-points, (b) top and side view of equilibrium structure of the monolayer $ZrSe_2$, (c) band structure, (d) total DOSs of the monolayer $ZrSe_2$, (e) top and side view of the equilibrium structure of the monolayer Nb-$ZrSe_2$, (f) band structure of the monolayer Nb-$ZrSe_2$, (g) total DOSs of the Nb-$ZrSe_2$, and (h) contribution of the d subshell of Nb in the total DOSs.

monolayer $ZrSe_2$ and Nb-$ZrSe_2$ materials. Analysis of the electronic properties can be useful to obtain information about electron distribution on the catalytic surface, which is useful to understand fully the catalytic performance of the catalyst. The electronic properties of the 2D monolayer $ZrSe_2$ and Nb-$ZrSe_2$ materials have been obtained by employing the same DFT-D theory. The electronic band structure of the pristine $ZrSe_2$ were plotted in the highly symmetric k-path direction Γ-*M*-*K*-Γ


https://doi.org/10.1021/acsphyschemau.3c00035
ACS Phys. Chem Au 2024, 4, 40−56

with respect to vacuum. The highly symmetric path is shown in Figure 3a and the equilibrium electronic structure of the 2D monolayer $ZrSe_2$ material is shown in Figure 3b (top and side view). The Fermi energy level ($E_F$) of the pristine $ZrSe_2$ was found at the energy value of −5.34 eV as shown by the dotted line in Figure 3c and d. The 2D single layer $ZrSe_2$ material shows semiconducting characteristics with the indirect band gap of about 1.48 eV as represented in Figure 3c. The DOSs have been computed by the same level of DFT-D theory, and the profile of DOSs supports the band gap of the 2D pristine $ZrSe_2$ which was obtained by the electronic band structures calculations as shown in Figure 3d. The calculated electronic band gap of the pristine 2D $ZrSe_2$ is consistent with the previously reported values.[39,40] Doping Nb in the pristine 2D monolayer $ZrSe_2$ (Nb-$ZrSe_2$) disrupts its symmetry and introduces additional unsaturated electrons. The equilibrium structure with the electronic properties of the 2D Nb-$ZrSe_2$ have been calculated at its equilibrium geometry by using the same level of the DFT-D theory as depicted in Figure 3e−g. This alteration leads to an augmented charge density in the basal plane of the 2D monolayer Nb-$ZrSe_2$ resulting in enhanced catalytic activity toward ORR. We have drawn the electronic band structure of the 2D Nb-$ZrSe_2$ along the highly symmetric k-path direction Γ-*M*-*K*-Γ like the pristine 2D monolayer $ZrSe_2$ material with respect to the vacuum for comparison. The $E_F$ of the 2D Nb-$ZrSe_2$ was found at −4.87 eV as represented by the dotted line in Figure 3f−h. The results from our present DFT-D analysis demonstrate that the introduction of Nb doping in the pristine 2D monolayer $ZrSe_2$ causes the energy gap to disappear, stemming in a zero-band gap where the bands are overlapped around the $E_F$ making it conductor. In other words, the 2D Nb-$ZrSe_2$ has metallic characteristics as shown in Figure 3f. The zero-band gap indicates easier electron transfer from the valence band to the conduction band. To support this, we computed the DOSs calculations using the same level of DFT-D theory. The DOSs profile shows that there is sufficient carrier concentration about the $E_F$ as shown in Figure 3g. An increased concentration of electrons near the $E_F$ enhances electronic conductivity, thereby facilitating faster electron transfer to the reactants during the process of ORR. The carrier density around the $E_F$ mostly comes from the dopant (Nb) **d**-subshell electron density of states. Based on our analysis of partial density of states (PDOS) calculations, we have successfully established the influence of the **d**-subshell electron density of states of the Nb atom on the carrier concentration around the $E_F$, as depicted in Figure 3h. The contributing component of the **d**-subshell electron density of the Nb atom in the total DOSs has been computed to examine the conducting properties of the material where the **d**-subshells electron density of states of the Nb atom follow the locus of the total DOSs of the 2D monolayer Nb-$ZrSe_2$ material. In other words, this indicates that the **d**-subshell electrons of the Nb atom regulates and tunes the electronic properties of the 2D monolayer Nb-$ZrSe_2$ material which may enhance the electrocatalytic activities of the material.

The distinctive electronic characteristics of the 2D monolayer Nb-$ZrSe_2$ can be summarized as follows: (1) the rapid transfer of charges is facilitated by the presence of continuous band states in close proximity to the $E_F$; (2) enhanced electron mobility can be observed due to the significant density of states surrounding the $E_F$; (3) the metallic properties of the 2D monolayer Nb-$ZrSe_2$ contribute to accelerate charge transfer leading to improve the ORR activity.

Considering the previous studies of the ORR mechanism on TMDs, the surface chalcogen atomic layer takes part in the reduction process of the molecular oxygen ($O_2$). Recently Upadhyay and Pakhira investigated the ORR mechanism on the surface chalcogen (Se) atomic layer of the 2D monolayer Pt-$MoSe_2$ using DFT-D methods.[27] So, in the case of TMDs, it can be concluded that the surface chalcogen atomic layer is the active center of the catalyst during the electrochemical ORR mechanism. In this work, we have investigated the ORR mechanism in an acidic media, where the protons ($H^+$) and electrons ($e^-$) transfer take place simultaneously on the ORR adsorbates to reduce the $O_2$. We considered the Se site as an active site (near the Nb-doped region) for the ORR adsorbates including the $O_2$*, 2O*, OOH*, O*, and OH*.

The ORR mechanism was started by analyzing the interaction of $O_2$ with the active site Se of the 2D monolayer Nb-$ZrSe_2$. The adsorption of $O_2$ with the active site is the crucial step to initiate the ORR process and significantly affects the catalytic activity of the material. Here, we calculated the adsorption energy of the $O_2$ molecule by taking the difference between the electronic energy of the absorbed Nb-$ZrSe_2$ of the $O_2$ denoted by the $O_2$*_Nb-$ZrSe_2$ with the electronic energy of isolated 2D Nb-$ZrSe_2$ and the gaseous state of the $O_2$ molecule. The adsorption energy of $O_2$ should not be too positive or too negative for a good electrocatalyst.[27,62,69,70] The higher positive adsorption energy value between $O_2$ and the active site (called the $O_2$-active site interaction) depicts that it is not able to capture the $O_2$ molecule. In other words, the higher and positive value of $O_2$ adsorption energy (around the active center) leads to poor adsorption of $O_2$ molecules, so it is very difficult to start the ORR process. A very negative adsorption energy value between $O_2$ and catalyst is not ideal for ORR mechanism because a very strong $O_2$-active site interaction may lead to occupation of active site by $O_2$ molecule and hinders the further reaction steps.[27,62,69,70] Thus, very large positive and negative values of the $O_2$ adsorption energy around the active site of the catalyst diminish the electrocatalytic activity of the material toward the ORR process. So, the adsorption energy of $O_2$ should be optimum to efficiently start the ORR on the catalytic surface. Based on the above discussion, we computed the $O_2$ activation energy, which could be good descriptor of the catalytic activity of the 2D monolayer Nb-$ZrSe_2$ toward ORR. In other words, the determination of the optimal value of $O_2$ adsorption energy on the Nb-$ZrSe_2$ surface plays a crucial role in initiating the ORR process. For an ideal condition, the adsorption energy of $O_2$ on the catalytic surface should be close to zero, which is not the case in real life. Noble metals, such as Pt are considered the best catalyst to date for electrochemical reactions especially for ORR. So, for practical applications the $O_2$-active center interaction energy for a good catalytic candidate should be close to or slightly weaker than that of the Pt. Chen et al. reported that the Pt-based catalyst shows good ORR reactivity, therefore, can be used as a reference to evolute the catalytic activity of other materials. The $O_2$ adsorption energies on the Pt (111) and Pt (100) surfaces were found to be −0.69 eV and −1.10 eV, respectively.[6,71] It was found in the present calculations that $O_2$ adsorption energy on the surface of the 2D monolayer Nb-$ZrSe_2$ was about −0.15 eV which is smaller than that of the $O_2$-active site interaction energy of Pt. Thus, this negative and small adsorption energy of $O_2$ suggests that


https://doi.org/10.1021/acsphyschemau.3c00035
ACS Phys. Chem Au 2024, 4, 40−56

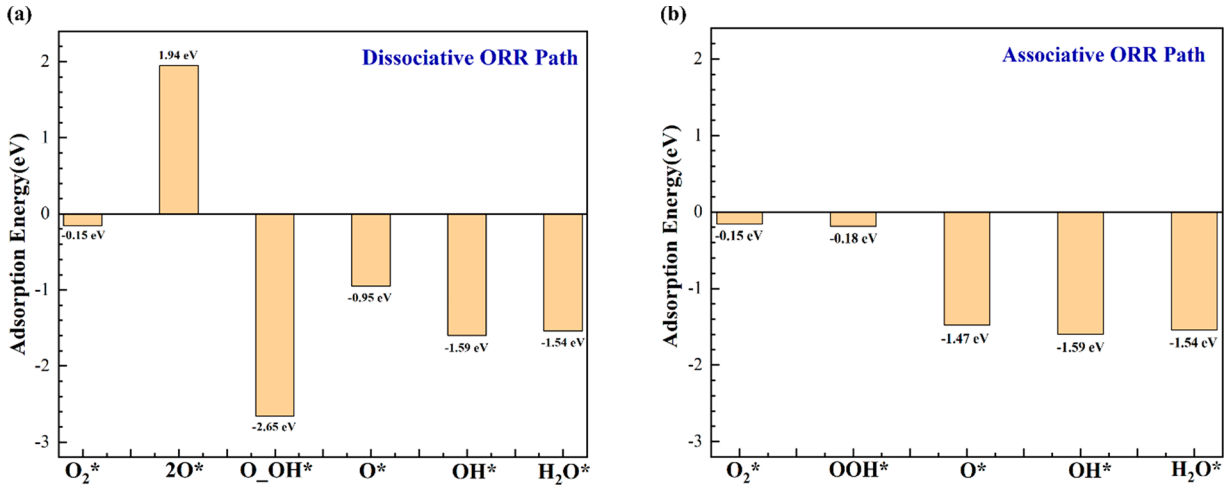


**Figure 4.** Graphical representation of adsorption energy of the various ORR intermediates in (a) dissociative and (b) associative mechanism.

the 2D monolayer Nb-$ZrSe_2$ can be energetically favorable for electrochemical ORR to proceed further, which indicates that the 2D monolayer Nb-$ZrSe_2$ material would show an efficient catalytic activity toward ORR.

Now, the removal of the water ($H_2O$) molecule is the last step of the ORR mechanism. After the removal of the $H_2O$ molecule, the new ORR cycle of the ORR mechanism starts. So, suitable $H_2O$ adsorption energy is essential during the ORR mechanism. The adsorption energy of $H_2O$ on the catalytic site should not be too large. The adsorption energy of $H_2O$ molecule was found to be −1.54 eV on the Se-site as represented in Figure 4. This value might seem like a moderate adsorption energy (not too large) in one context, and it could actually be favorable for a particular reaction mechanism, as in the case of the subject reaction. This value may not appear extremely small in isolation; it is indeed a suitable moderate value for the ORR mechanism. This value supports the efficient adsorption, reaction, and subsequent desorption of $H_2O$ molecules, enabling the catalytic site to remain accessible and active throughout multiple cycles of the ORR. This means that the Se site remains accessible for the subsequent cycles of the ORR. Moreover, the favorable adsorption energies of $O_2$ and $H_2O$ on the Se site of the 2D Nb-$ZrSe_2$ indicates that this material has the potential to serve as an effective catalyst for converting $O_2$ into $H_2O$ during the reduction process.

Now, after the adsorption of the $O_2$ molecule, which is the initial step of the ORR mechanism, ORR can proceed via two ways. The path of the ORR mechanism depends on how the O═O bond cleaves. The first way is called associative path, which involves both the proton and electron transfer simultaneously to form OOH species, then followed by the successive protonation steps to reduce $O_2$. The second path is known as the dissociative path, which involves the breaking of the O═O bond after the adsorption of the $O_2$ molecule into two O atoms on the active site of the catalytic surface. In this work, we have studied both possible pathways of the ORR mechanism on the surface of the 2D monolayer Nb-$ZrSe_2$. We computed the adsorption energy of the reaction intermediates with the active site Se of 2D Nb-$ZrSe_2$ for both associative and dissociative reaction pathways. The adsorption energy for the hydrogenation of $O_2$* into the OOH* species during the associative reaction was found to be −0.18 eV obtained by the DFT-D calculation as represented in Figure 4b. The adsorption energy of the dissociative pathway (i.e., dissociation of the adsorbed $O_2$* into 2O*) was found to be 1.94 eV, i.e., the dissociation energy of $O_2$*. According to computed adsorption energy, the associative pathway is more energetically favorable than that of the dissociative pathway. The adsorption energy for the associative pathway ($O_2$* → OOH*) indicates that the OOH* species is stably adsorbed on the Se site of the 2D Nb-$ZrSe_2$. As the adsorption energy of associative path (−0.18 eV) is close to zero i.e., very small and negative, therefore, we consider the associative ORR path would be thermodynamically favorable and feasible. Thus, we believe that the associative reaction path is energetically more favorable and efficient for catalyzing $O_2$ molecules. The associative reaction path is represented as $O_2$* + $H^+$ + $e^-$ → OOH*. The large positive adsorption energy of dissociation of the $O_2$ molecule to the atomic O indicates that this step is not stable and would be greatly suppressed by the associative $4e^-$ mechanism. A positive adsorption energy implies that the dissociation of $O_2$ is not energetically favorable, which hinders the progression of subsequent reaction steps. So, the whole ORR mechanism will proceed as $O_2$* → OOH* → O* + $H_2O$ → OH* → $H_2O$. The adsorption energy of all ORR intermediates has been calculated by the same level of theory. The graphical representation of the adsorption energy of all intermediate steps is shown in Figure 4a-b. For all the intermediates states involved in the associative path, the adsorption energy is negative and optimum, revealing highly exothermic characteristics and thermodynamically favorable. We also computed the adsorption energy for all the ORR intermediates that occur in the dissociative ORR pathway as represented in Figure 4a.

From the above discussion, we can conclude that the ORR mechanism on the surface of the 2D monolayer Nb-$ZrSe_2$ material will follow the $4e^-$ associative mechanism. To further analyze the catalytic activity of the 2D monolayer Nb-$ZrSe_2$ toward ORR, we have computed the values of $\Delta G$ for each intermediate reaction steps. In this work, we have calculated the values of $\Delta G$ by computing the harmonic vibrational frequency of each intermediate step of ORR mechanism using the CRYSTAL17 code. We will discuss the $\Delta G$, structural properties, and electronic properties of each reaction intermediate step involved in both associative and dissociative mechanism during the ORR.


https://doi.org/10.1021/acsphyschemau.3c00035
ACS Phys. Chem Au 2024, 4, 40−56

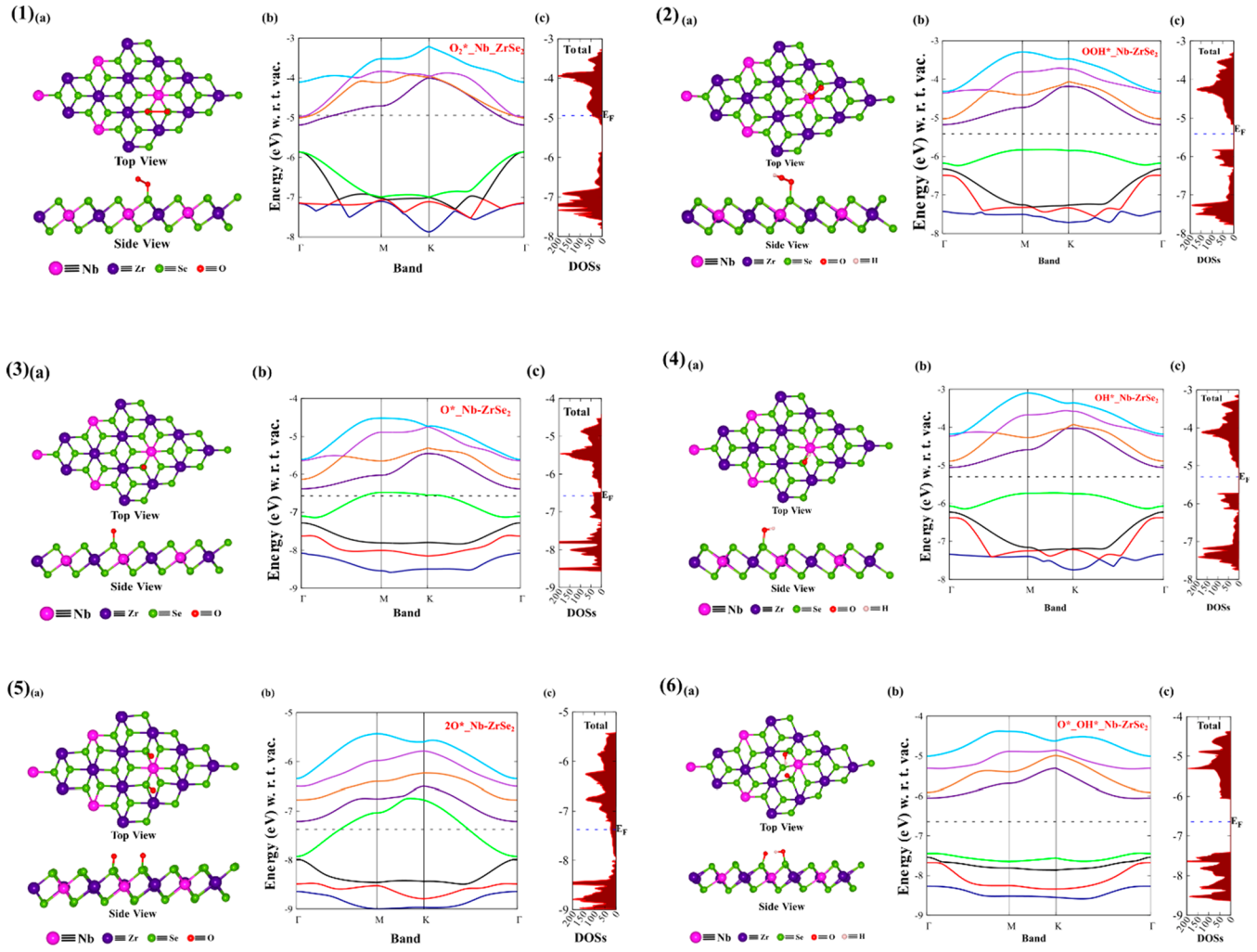


**Figure 5.** Top and side view of equilibrium structure, (b) band structure, and (c) total DOSs of (1) $O_2$*_Nb-$ZrSe_2$, (2) OOH*_Nb-$ZrSe_2$, (3) O*_Nb-$ZrSe_2$, (4) OH*_Nb-$ZrSe_2$, (5) 2O*_Nb-$ZrSe_2$, and (6) O*_OH*_Nb-$ZrSe_2$.

## Reaction Intermediate Steps Involved in Associative Mechanism

**First Step.** The first step of the ORR mechanism, irrespective of the path, is the adsorption of $O_2$ onto the reaction site of the 2D monolayer Nb-$ZrSe_2$ slab. To model this step, we placed an $O_2$ molecule on the surface near to the Nb atom in the 2D Nb-$ZrSe_2$ at a distance 1.60 which is equal to the equilibrium bond length of the Se−O. The same DFT-D method has been employed to perform the geometry optimization of the 2D Nb-$ZrSe_2$ with an $O_2$ molecule attached to the Se site (represented as $O_2$*_Nb-$ZrSe_2$). The equilibrium structure of the $O_2$*_Nb-$ZrSe_2$ has been represented in Figure 5(1a) (top and side view). We analyzed and calculated the intrinsic electronic characteristics of the equilibrium structure $O_2$*_Nb-$ZrSe_2$. In order to gain insights into the electronic properties, we calculated the electronic band structure and DOSs of the equilibrium structure $O_2$*_Nb-$ZrSe_2$ as depicted in Figure 5(1b) and 5(1c), respectively. We plotted a total of eight bands around the $E_F$, which are sufficient for collecting the electronic behavior of the $O_2$*_Nb-$ZrSe_2$. We calculated the band structure of the $O_2$*_Nb-$ZrSe_2$ along the Γ-*M*-*K*-Γ high symmetry *k*-vector direction with respect to vacuum, which is consistent to the 2D Nb-$ZrSe_2$ band structure with the band pathway along the same *k*-vector direction for comparison. The $E_F$ was found at −4.94 eV as represented by the dotted line in Figure 5(1b-c). From the band structure calculations, we observed that some of the electronic bands overlap around the $E_F$. Thus, the band structure of the $O_2$*_Nb-$ZrSe_2$ predicts the conducting nature of the $O_2$*_Nb-$ZrSe_2$ system. To confirm the conducting nature of the $O_2$*_Nb-$ZrSe_2$, we computed and analyzed the DOSs of the $O_2$*_Nb-$ZrSe_2$. According to the DOSs profile, there appears to be an ample amount of electron density surrounding the $E_F$ as shown in Figure 5(1c). Therefore, the intermediate $O_2$*_Nb-$ZrSe_2$ has metallic characteristics. After optimization, the equilibrium Se−O and O−O bond lengths were found to be 1.67 Å, and 2.20 Å, respectively. We observed an increased bond length of the O−O bond as compared to the free $O_2$ molecule bond length (1.21 Å) by the amount of 0.99 Å after the adsorption onto surface of the Nb-$ZrSe_2$ as represented in Figure 6. The type of oxygen molecule is crucial for ORR. Usually, $O_2$ molecules have two bond states, singlet ($^1O_2$, metastable) and triplet ($^3O_2$ ground state), where $^1O_2$ has a very short lifespan and has 0.98 eV higher energy than $^3O_2$.[72,73] Therefore, $O_2$ is involved in the oxygen electrocatalysis in fuel cells and the electrochemical water splitting is specifically considered to be completely in its triplet ground state.[74] The electron spin alignment facilitates the creation of


https://doi.org/10.1021/acsphyschemau.3c00035
ACS Phys. Chem Au 2024, 4, 40−56

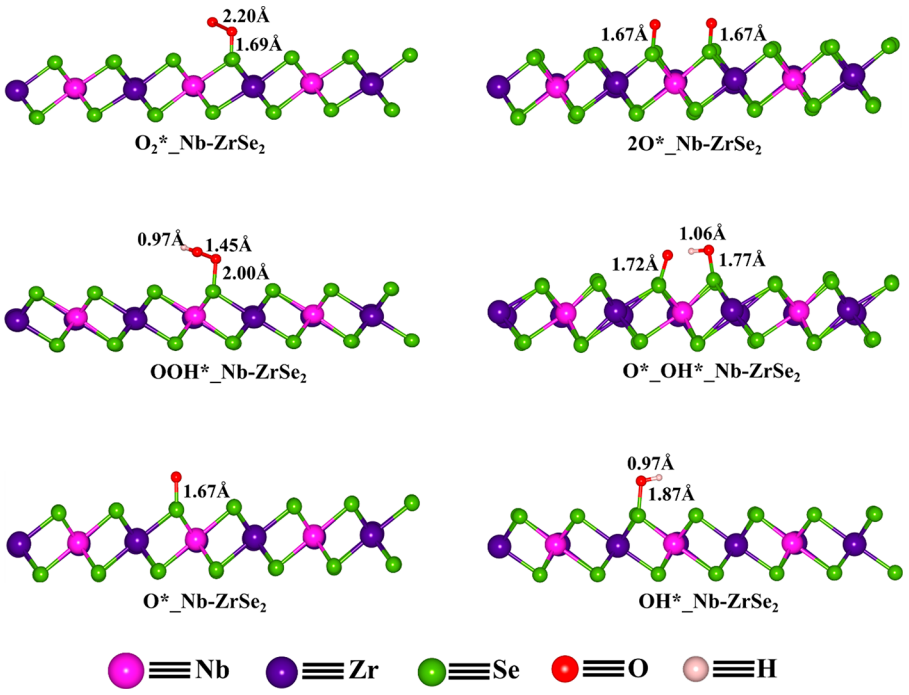


**Figure 6.** Structural properties of the various ORR intermediate structures.

**Table 2. Equilibrium Geometrical Data of the ORR Intermediates Involved on the Associative and Dissociative Mechanism**

| Reaction steps | Lattice parameters (Å) | Interfacial angle (deg) | Layer group and symmetry | Electronic band gap (eV) | Average bond length (Å) | | | |
|---|---|---|---|---|---|---|---|---|
| | | | | | Zr–Se | Nb–Se | Se–O | Se–OH |
| Nb-$ZrSe_2$ | $a$ = 7.38, $b$ = 7.38 | $\alpha = \beta = 90°$ $\gamma = 120°$ | *P1* | 0 | 2.67 | 2.60 | - | - |
| $O_2$*_Nb-$ZrSe_2$ | $a$ = 7.37, $b$ = 7.38 | $\alpha = \beta = 90°$ $\gamma = 120.01°$ | *P1* | 0 | 2.67 | 2.58 | 1.69 | - |
| 2O*_Nb-$ZrSe_2$ | $a$ = 7.39, $b$ = 7.35 | $\alpha = \beta = 90°$ $\gamma = 120.36°$ | *P1* | 0 | 2.66 | 2.60 | 1.67 | 1.67 |
| OOH*_Nb-$ZrSe_2$ | $a$ = 7.39, $b$ = 7.40 | $\alpha = \beta = 90°$ $\gamma = 120.20°$ | *P1* | 0.66 | 2.66 | 2.66 | 2.00 | - |
| O*_OH*_Nb-$ZrSe_2$ | $a$ = 7.39, $b$ = 7.43 | $\alpha = \beta = 90°$ $\gamma = 120.32°$ | *P1* | 1.39 | 2.68 | 2.61 | 1.72 | 1.77 |
| O*_Nb-$ZrSe_2$ | $a$ = 7.37, $b$ = 7.41 | $\alpha = \beta = 90°$ $\gamma = 120.13°$ | *P1* | 0 | 2.67 | 2.60 | 1.67 | - |
| OH*_Nb-$ZrSe_2$ | $a$ = 7.38, $b$ = 7.40 | $\alpha = \beta = 90°$ $\gamma = 120.10°$ | *P1* | 0.66 | 2.65 | 2.61 | 1.87 | - |

spin, a selective channel to promote spin conversion during the reaction which provides an opportunity to lower the reaction energy barrier by controlling the spin polarization of the catalyst.[75] The adsorption and activation of the triplet $O_2$ molecule should involve charge transfer from the catalytic site to the antibonding Π* orbital of $O_2$. Such an orbital interaction on our system arises from the interaction of the ligands Se site orbital of the Nb-$ZrSe_2$ and Π* orbital of adsorbed $O_2$ on the surface of the Nb-$ZrSe_2$. We have employed the Mulliken charge transfer analysis by including the "PPAN" and spin polarization calculation by including the keyword "SPIN" in the calculations. The optimized geometry of the $O_2$*_Nb-$ZrSe_2$ suggests the charge transfer of 0.64 |e| from the Se site to the adsorbed $O_2$ molecule. The charge transfer thus resulted in the elongation of the equilibrium bond length of the $O_2$ molecule to 2.20 Å as compared to the free optimized $O_2$ bond length (1.21 Å). Thus, the charge transfer and bond elongation of the $O_2$ molecule are responsible for the activation of the $O_2$ molecule on the surface of 2D Nb-$ZrSe_2$. The increment in the bond length and charge transfer indicates that the $O_2$ molecule is activated and is available for the next ORR steps. The value of $\Delta G$ during the reaction $O_2 + * \rightarrow O_2*$ was found to be −0.10 eV. The negative value of $\Delta G$ indicates that the reaction is exothermic. Thus, the negative and small value of $\Delta G$ suggests that the adsorption of $O_2$ on the active site is thermodynamically stable and kinetically feasible for the ORR mechanism.

**Second Step.** The next step (in the $4e^-$ transfer associative reaction mechanism of the subject reaction) is the hydrogenation of adsorbed activated oxygen molecule around the Se site near the Nb atom. To model this ORR intermediate, we have placed one H atom near to the one O atom and the present DFT-D study has found that the equilibrium O–H distance is about 0.97 Å from the outer O atom in the


https://doi.org/10.1021/acsphyschemau.3c00035
ACS Phys. Chem Au 2024, 4, 40–56

$O_2$*_Nb-$ZrSe_2$. Here, we assumed that a $H^+$ coming from the anode side through a proton exchange membrane and an $e^-$ coming through an external circuit reacts with the adsorbed $O_2$ molecule to form an OOH (noted by OOH*_Nb-$ZrSe_2$). The full geometry optimization (i.e., atomic coordinates and lattice parameters) of the so formed system of the OOH*_Nb-$ZrSe_2$ reaction intermediate was performed by employing the same DFT-D method, and the equilibrium structure of the OOH*_Nb-$ZrSe_2$ intermediate is shown in Figure 5(2a) (top and side view). We computed and examined the electronic properties of the OOH*_Nb-$ZrSe_2$ using the same DFT-D method. The $E_F$ was found at −5.42 eV as shown by the dotted line in Figure 5(2b−c). The band structures of the OOH*_Nb-$ZrSe_2$ depict the semiconducting nature of the OOH*_Nb-$ZrSe_2$ reaction intermediate with an indirect band gap of 0.66 eV. The conduction band minima and the valence band maxima of the OOH*_Nb-$ZrSe_2$ are located as Γ- and M- points, respectively. The DOSs corresponding to the band structures of the OOH*_Nb-$ZrSe_2$ were also calculated and plotted by using the same DFT-D method as shown in Figure 5(2c). The DOSs plot is very consistent with the band structures, and this computation supports the band gap of the OOH*_Nb-$ZrSe_2$ intermediate. The value of $\Delta G$ during the reaction $O_2$* + $H^+$ + $e^-$ → OOH* was found to be 0.13 eV. This positive value of the $\Delta G$ indicates the endothermic nature of the reaction. The value of $\Delta G$ is close to zero, which suggests a thermodynamically favorable process and proceeds for the further reaction steps.

**Third Step.** The next step of $4e^-$ associative mechanism is the reduction of OOH* into O* through the process of hydrogenation of the reaction intermediate OOH*_Nb-$ZrSe_2$. We assume that a proton ($H^+$) coming from the anode side through proton exchange membrane and simultaneously, electron ($e^-$) flow through an external circuit, reacts with OOH* to form O* intermediate species. We have modeled this intermediate state by placing an oxygen atom at a distance 1.62 Å from the Se site which is close to equilibrium bond length of Se−O. The full optimization (lattice parameters and atomic coordinates) of the reaction intermediate O*_Nb-$ZrSe_2$ was performed and the equilibrium 2D layer structure (top and side view) of the O*_Nb-$ZrSe_2$ is represented in Figure 5(3a). Figure 5(3b-c) represents the electronic band structure and DOSs profile of the O*_Nb-$ZrSe_2$ computed by the DFT-D method. The $E_F$ of the O*_Nb-$ZrSe_2$ system was found at −6.57 eV as shown by the dotted line in Figure 5(3b-c). From the band structure calculations of the O*_Nb-$ZrSe_2$ intermediate, it has been found that some of the energy bands cross the $E_F$, which indicates the metallic nature of the O*_Nb-$ZrSe_2$. The DOSs calculations of the O*_Nb-$ZrSe_2$ show that there is electron density around the $E_F$ as shown in Figure 5(3c). So, both the band structure and the DOSs profile show the metallic nature of the O*_Nb-$ZrSe_2$, which supports the transportation of electrons involved in this reaction step. The value of $\Delta G$ in this reaction step (OOH* → O*) was found to be −1.82 eV. The negative value of $\Delta G$ reveals a highly exothermic character of this reaction. This intermediate reaction step is thermodynamically stable and energetically favorable for ORR mechanism.

**Fourth Step.** The next step of $4e^-$ associative mechanism is the hydrogenation of the O*_Nb-$ZrSe_2$ intermediate by reacting with $H^+$ and $e^-$ coming from the anode side of the fuel cell. We assume that O* at the Se site captures one $H^+$ and $e^-$ to form OH* species. To model this intermediate state, we put an H atom at a distance 0.90 Å from the O atom, which is equilibrium bond distance of a free O−H molecule. The reaction intermediate OH*_Nb-$ZrSe_2$ was then optimized and the equilibrium structure of the OH*_Nb-$ZrSe_2$ intermediate is illustrated in Figure 5(4a). To examine the electronic behavior, we studied the electronic properties of the OH*_Nb-$ZrSe_2$ intermediate. The $E_F$ of the OH*_Nb-$ZrSe_2$ was found at −5.30 eV as depicted by the dotted line in Figure 5(4b-c). From the band structure calculations, we can see that the OH*_Nb-$ZrSe_2$ displays semiconducting nature with the indirect band gap of 0.66 eV as shown in Figure 5(4b). The conduction band minima and the valence band maxima of the OH*_Nb-$ZrSe_2$ are located at Γ and M, respectively, like the previous intermediate step. To confirm this band gap, we drawn the DOSs profile corresponding to the band structure calculations, and the DOSs profile well supports the band gap of the OH*_Nb-$ZrSe_2$ as shown in Figure 5(4c). The value of $\Delta G$ for this reaction step (O* → OH*) was found to be −1.23 eV computed by the same DFT-D method. The negative value of $\Delta G$ indicates that this step is exothermic, and hence, this process is thermodynamically and energetically favorable for the reduction of $O_2$.

**Fifth Step.** This is the last step of the ORR mechanism. This step of the $4e^-$ associative mechanism is the hydrogenation of the OH*_Nb-$ZrSe_2$ intermediate by reacting with $H^+$ and $e^-$ coming from the anode side of the fuel cell. We assume that the OH* at the Se site captures one $H^+$ and $e^-$ to form the second $H_2O$ molecule and it is removed from the catalytic site. The value of the $\Delta G$ of this reaction step (OH* → $H_2O$ + *) was found to be −1.76 eV computed by the same DFT-D method. The negative value of $\Delta G$ indicates that this ORR step is exothermic, and hence, this process is thermodynamically and energetically favorable for the reduction of $O_2$. The value of $\Delta G$ of each reaction intermediate during the associative mechanism has been reported in Table 3, and similarly, the value of $\Delta G$ of each reaction intermediate during the dissociative mechanism has been reported in Table 4. The geometrical data of each of the intermediate structures after the optimization has been

**Table 3. Change in Gibbs Free Energy (eV) of the Reaction Steps during the Associative Mechanism at the Surface of the 2D Monolayer Nb-$ZrSe_2$ Material**

| Various reaction steps involved in associative mechanism | $\Delta G$ (eV) |
|---|---|
| [Nb-$ZrSe_2$ + $O_2$ → $O_2$*_Nb-$ZrSe_2$] | −0.28 |
| [$O_2$*_Nb-$ZrSe_2$ + $H^+$ + $e^-$ → OOH*_Nb-$ZrSe_2$] | 0.13 |
| [OOH*_Nb-$ZrSe_2$ + $H^+$ + $e^-$ → O*_Nb-$ZrSe_2$ + $H_2O$] | −1.82 |
| [O*_Nb-$ZrSe_2$ + $H^+$ + $e^-$ → OH*_Nb-$ZrSe_2$] | −1.23 |
| [OH*_Nb-$ZrSe_2$ + $H^+$ + $e^-$ → Nb-$ZrSe_2$ + $H_2O$] | −1.76 |

**Table 4. Change in Gibbs Free Energy of Reaction Steps in the Dissociative Mechanism at the Surface of the 2D Monolayer Nb-$ZrSe_2$ Material**

| Various reaction steps involved in dissociative mechanism | $\Delta G$ (eV) |
|---|---|
| [Nb-$ZrSe_2$ + $O_2$ → $O_2$*_Nb-$ZrSe_2$] | −0.28 |
| [$O_2$*_Nb-$ZrSe_2$ → 2O*_Nb-$ZrSe_2$] | 1.99 |
| [2O*_Nb-$ZrSe_2$ + $H^+$ + $e^-$ → O*_OH*_Nb-$ZrSe_2$] | −2.26 |
| [O*_OH*_Nb-$ZrSe_2$ + $H^+$ + $e^-$ → O*_Nb-$ZrSe_2$ + $H_2O$] | −1.40 |
| [O*_Nb-$ZrSe_2$ + $H^+$+$e^-$ → OH*_Nb-$ZrSe_2$] | −1.23 |
| [OH*_Nb-$ZrSe_2$ + $H^+$ + $e^-$ → Nb-$ZrSe_2$ + $H_2O$] | −1.76 |


https://doi.org/10.1021/acsphyschemau.3c00035
ACS Phys. Chem Au 2024, 4, 40−56

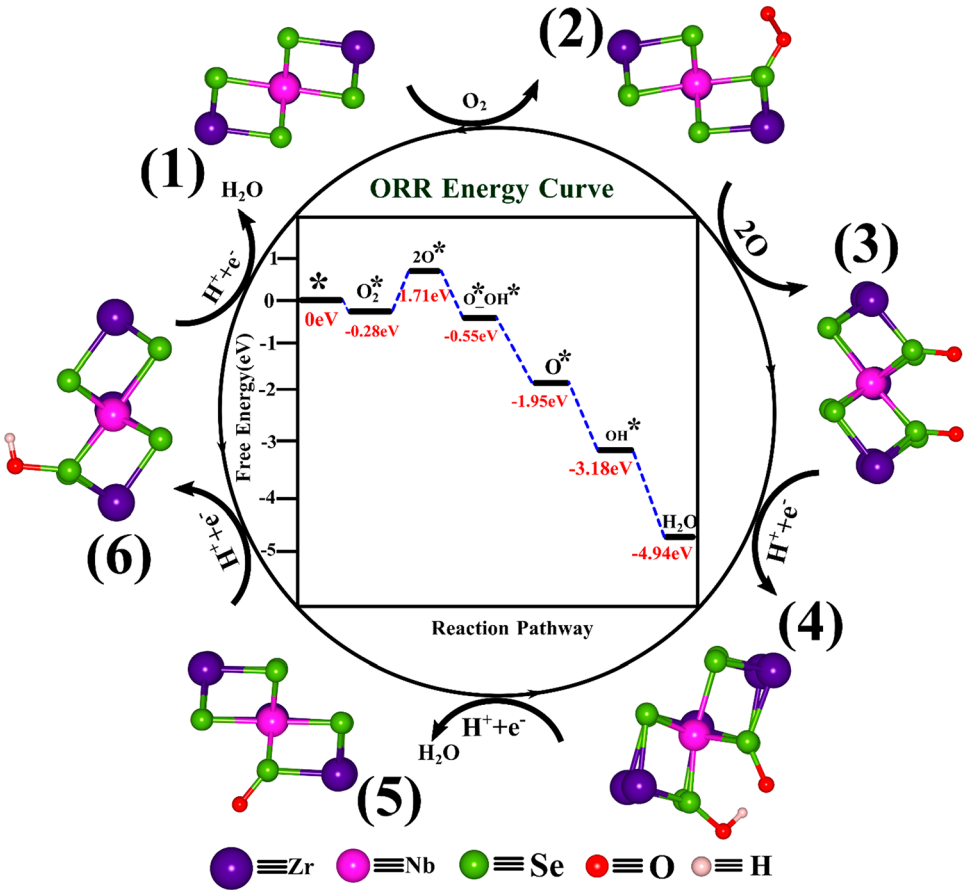


**Figure 7.** Free energy diagram of the dissociative ORR mechanism at the surface of the 2D monolayer Nb-$ZrSe_2$ material.

summarized in Table 2 and represented in Figure 6 (for both associative and dissociative mechanism). A detailed explanation of the dissociative path of the ORR mechanism on the surface of the Nb-$ZrSe_2$ can be found in SI.

To summarize the catalytic activity of the 2D Nb-$ZrSe_2$ toward ORR, we plotted and analyzed the $\Delta G$ curve (potential energy curve) for both associative and dissociative mechanism based on the DFT-D calculations as shown in Figures 7 and 8. We constructed these diagrams by considering the 2D Nb-$ZrSe_2$ as a reference geometry, i.e., 2D Nb-$ZrSe_2$ considered corresponding to energy of 0 eV for both associative and dissociative mechanism of ORR. At a standard condition (i.e., at a temperature of 298.15 K with pressure 1 atm) the total value of $\Delta G$ for full reaction $O_2 + 2H_2 \rightarrow 2H_2O$ should be −4.92 eV. From our Gibbs energy landscape, the total value of $\Delta G$ was found to be −4.94 eV and −4.96 eV for dissociative and associative mechanism, respectively. So, from our DFT-D calculations we can see that total value of $\Delta G$ for the ORR mechanism is very consistent with the experimental value. In dissociative path, the free energy landscape shows that all the reaction steps are downhill except $O_2^* \rightarrow 2O^*$ as shown in Figure 7. For the associative path, all of the reaction steps are also downhill in the free energy landscape except for the reaction steps for $O_2^* \rightarrow OOH^*$ as shown in Figure 8. But by comparing both the free energy landscape, the $O_2^* \rightarrow 2O^*$ step of the dissociative mechanism has higher uphill than that of the associative mechanism. Thus, the 2O* step is not stable and thermodynamically feasible for ORR mechanism, which makes the further ORR steps through dissociative path difficult. Whereas the uphill in associative mechanism is very small which is kinetically surmountable. Furthermore, all values of $\Delta G$ are negative, indicating that the entire ORR process through associative mechanism is exothermic and thermodynamically favorable. Therefore, the associative $4e^-$ pathway for the ORR on the surface of 2D Nb-$ZrSe_2$ is the most favorable path.

The potential energy surface for both the associative and dissociative paths has been discussed for the sake of a quick comparison of results in both mechanisms. The total values of $\Delta G$ for two reaction pathways (4.94 eV for the dissociative ORR mechanism and 4.96 eV for the associative mechanism) are marginally different (only 0.02 eV), which lies in the DFT-D error bar. This slight difference in the total value of $\Delta G$ for two reaction pathways might come from the different reaction energies (i.e., the different interaction strengths) of different intermediate species occurring on both the associative and dissociative mechanisms. The specific bond-breaking and bond-formation steps in a different pathway may possess distinct reaction energies due to variations in the bond strength, atomic interactions, and stabilities of intermediates, ultimately affecting the calculated total $\Delta G$ values. In our calculations, the reaction energies of $O_2^* \rightarrow 2O^*$ and $O_2^* + H^+ + e^- \rightarrow OOH^*$ were found to be 1.94 eV and −0.18 eV, respectively. Another factor is the change in the entropy during each process that contributes to the overall value of $\Delta G$. Different changes in entropy arise from different reaction mechanisms and different translational and variational degrees of freedom of intermediate species (2O* and OOH*). In the


https://doi.org/10.1021/acsphyschemau.3c00035
ACS Phys. Chem Au 2024, 4, 40−56

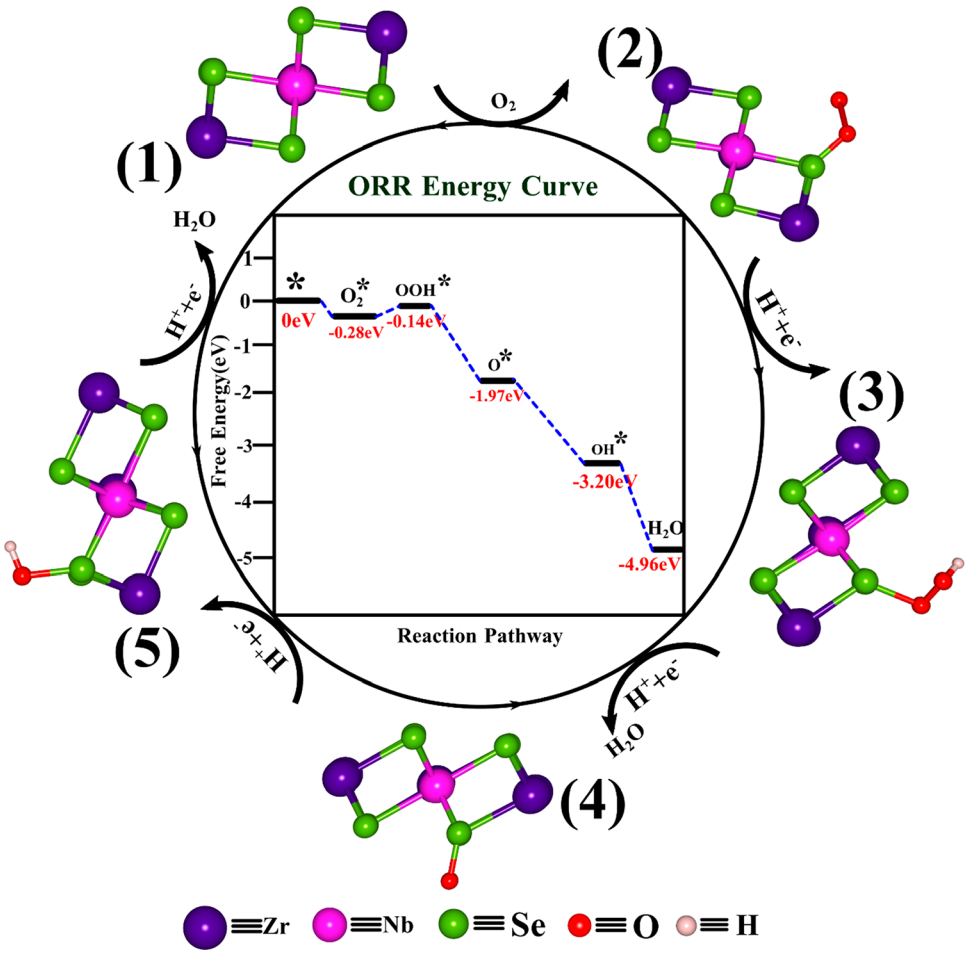


**Figure 8.** Free energy diagram of the associative ORR mechanism at the surface of the 2D monolayer Nb-$ZrSe_2$ material.

context of electrocatalytic reactions, the concept of entropy helps us to understand how the arrangement of molecules and their energy distribution change as a reaction proceeds. When molecules transition from reactants to products, their spatial arrangement and energy distribution can change, leading to differences in entropy. Besides these factors, the rate of electron transfer differs between reaction pathways due to variations in the redox potential of intermediates and the effect on the total $\Delta G$ values. Thus, the reaction energies, electron transfer rate, and entropy contribution of different reaction intermediates may cause minor differences in the values of $\Delta G$ during both associative and dissociative reaction mechanisms. The difference in $\Delta G$ is only about 0.02 eV which is negligible and lies in the DFT-D error bar.

In the case of the 2D monolayer Nb-$ZrSe_2$, the value of $\eta$ has been determined to be 1.09 V for the associative reaction path of the ORR. The overpotential of the benchmark Pt (111) was calculated to be 0.45 V at the same level of theory.[9] This discrepancy indicates that the 2D monolayer Nb-$ZrSe_2$ requires a higher driving potential to achieve the desired ORR rate compared to Pt. This observation suggests that the 2D monolayer Nb-$ZrSe_2$ might not be as efficient as Pt (111) as a cathode material for ORR; however, this material can be used as a Pt-free electrocatalyst where the performance is remarkable. To provide a comprehensive comparison, we considered some of the 2D surfaces such as 2D transition-metal-based, organic framework-based materials, and Pt-doped transition metal dichalcogenides. Recently, S. N. Upadhyay and S. Pakhira reported that the Pt doped $MoSe_2$ (Pt-$MoSe_2$) 2D transition metal dichalcogenides is an efficient electrocatalyst for ORR by employing the same level of theory. They computationally showed that the 2D transition metal dichalcogenides possess the value of $\eta$ about 1.53 V, which is higher than that of the overpotential of 2D single layer Nb-$ZrSe_2$ material.[27] Zhau et al. studied the efficiency of double carbon vacancy $C_3N$ monolayer with embedded a range of transition metals denoted by TM-$V_{cc}$ (TM = Mn, Fe, Co, Cu, Ru, Rh, Pd, and Pt) toward ORR.[76] The overpotential of the Nb-$ZrSe_2$ is quite near most of the TM-$V_{cc}$ catalysts. Furthermore, Ji et al. counted the first principle calculations to investigate the catalytic performance of the 2D M-COFs (M = Sc, Zn, Ru, Pd, Ag, and Ir).[77] According to their findings, most of the M-COFs represent an overpotential comparable to that of the 2D monolayer Nb-$ZrSe_2$. The overpotential of the 2D monolayer Nb-$ZrSe_2$ is comparable to various previously reported 2D materials overpotential studied using the DFT method for ORR catalyst.[78,79]

While the lower value of overpotential comparable to that of the Pt catalyst suggests an enhanced catalytic activity, it is important to consider other factors to evaluate catalytic efficacy. As 2D monolayer Nb-$ZrSe_2$ possesses a conducting nature, it facilitates the charge transfer and the ORR happens on the surface of the Nb-$ZrSe_2$; hence, it provides more exposure to the active catalytic sites, providing more opportunities for the ORR to take place. The availability and sustainability of the constituent elements, Nb, Zr, and Se, and


https://doi.org/10.1021/acsphyschemau.3c00035
ACS Phys. Chem Au 2024, 4, 40−56

the cost-effectiveness of the Nb-$ZrSe_2$ in comparison to precious metals like Pt present ecological and economically viable alternatives for large-scale applications. Our finding shows that the 2D monolayer Nb-$ZrSe_2$ exhibits good selectivity for the favorable reaction path and moderate adsorption energy of the ORR intermediates on the catalytic surface. The unique structural and electronic properties, stability, cost-effectiveness, and path selectivity of the 2D monolayer Nb-$ZrSe_2$ for ORR collectively positioned it as a promising catalyst for ORR, despite a slightly higher overpotential.

The study of the ORR is a solid surface reaction, and it happens on the outer surface of the 2D layer of the Nb-$ZrSe_2$ TMD. The examination of solvent impact holds significant relevance within the realm of catalysis. Additionally, gaining insights into the reaction mechanisms occurring on the solvent phase for various electrochemical reactions presents an equally interesting and important area of research study. Achieving a precise representation of the solvent model stands as a significant challenge within the realm of computational catalysis. Furthermore, the computational expense associated with modeling the various reaction steps (in the solvent phase) exacerbates this challenge.[80,81] When considering a solvent environment, it becomes apparent that the solvent possesses the capability to interact with the adsorbates and the catalytic surface through either chemical or physical processes. Notably, the solvent molecules can interact with adsorbates by hydrogen bonding. The effects of the solvent phase are very challenging owing to the difficulties in accurately defining complex systems that may involve simultaneous solvent−solvent, adsorbate-solvent, adsorbent-solvent, and adsorbate-catalytic surface interactions. The primary focus revolves around precisely defining the interaction potential and the exchange-correlation functionals involved in the solvent phase. Introducing the solvent phase introduces complexity, often resulting in expansive systems characterized by numerous feasible thermodynamic and geometrical arrangements. Consequently, the task of identifying a relevant configuration becomes equally challenging. In addition to this, the solvent phase is the main component of the reaction medium. Consequently, its physical attributes such as polarity, viscosity, and propensity to interact with adsorbates play a transformative role in influencing reaction kinetics through their impact on both mass and heat transfer phenomena. Thus, the task of precisely understanding how the inherent properties of the solvent influence the reaction dynamics is far from straightforward. Owing to these complications, the solvent phase is neglected by the researchers in DFT calculations, instead approximating it using vacuum or gas-phase conditions, and moreover, we took the relative energy changes during the reactions where the solvation effects are negligible.[82] Because of computational limitations, we did not include calculations for the solvent phase in this study as the relative values of $\Delta G$ have been considered in the present investigation, and such big calculations should be left for future study.

## CONCLUSIONS

In conclusion, we theoretically shed light on the geometrical structure, electronic properties, and catalytic activity of the 2D monolayer Nb-$ZrSe_2$ material as well as the detailed ORR mechanism on the surface of the 2D Nb-$ZrSe_2$ by using the DFT-D method. We investigated and examined both the possible path, i.e., associative and dissociative path, of the ORR mechanism on the surface of the 2D Nb-$ZrSe_2$. The analysis of the electronic properties of pure monolayer $ZrSe_2$ demonstrated that a single layer of $ZrSe_2$ in a two-dimensional form exhibits semiconductor behavior, characterized by a band gap of 1.48 eV. To alter the electronic properties and catalytic activity of the $ZrSe_2$, the substitutional doping of Nb has been done per 2 × 2 supercell of the $ZrSe_2$ monolayer. The 2D monolayer Nb-$ZrSe_2$ material has a zero band gap, indicating the metallic nature of the 2D Nb-$ZrSe_2$. Conductivity of the 2D monolayer Nb-$ZrSe_2$ material plays a crucial role in facilitating the movement of electrons in the mechanism of ORR and 2D Nb-$ZrSe_2$ could act as an excellent catalyst toward ORR. To analyze the whole reaction process, ORR intermediate structures involved in the associative and dissociative path were constructed and optimized by using the same DFT-D method. To examine the catalytic activity, we computed the adsorption energy of ORR intermediates involved in both associative and dissociative mechanism. The dissociative mechanism involves the following intermediates $O_2^* \rightarrow 2O^* \rightarrow O^*\_OH^* \rightarrow O^* + H_2O \rightarrow OH^*$ and associative mechanism has the following intermediates $O_2^* \rightarrow OOH^* \rightarrow O^* + H_2O \rightarrow OH^*$. For the dissociative mechanism, the value of $\Delta E$ of 2O* intermediate was found to be 1.99 eV to the catalytic site on the surface of the 2D Nb-$ZrSe_2$, which indicates poor binding of 2O*. For the associative mechanism, the value of $\Delta E$ of the OOH* intermediate was found to be −0.18 eV, which indicates the optimum binding of the OOH* to the catalytic site on the surface of the 2D Nb-$ZrSe_2$. Thus, the dissociative path would be a less favorable path to reduce the $O_2$ molecule to water as compared to that of the associative path. In addition, for associative mechanism the value of $\Delta E$ for all intermediates is negative. The negative value of $\Delta E$ indicates that all the intermediates have good binding with Se site, thus energetically favorable path. The value of $\Delta G$ for all the reaction intermediates has also been computed. The values of $\Delta G$ also suggests that the associative path would be preferred over the dissociative mechanism. Thus, 2D Nb-$ZrSe_2$ can be used as an excellent catalyst for the ORR mechanism.

## ASSOCIATED CONTENT

### Data Availability Statement

This work was carried out with the following version of the programs. All the structures were modeled by using the VESTA software. (https://jp-minerals.org/vesta/en/) All the calculations were carried out by using the *ab-initio* based CRYSTAL17 suite code. (https://www.crystal.unito.it/) GNUPLOT and Inkscape 0.92 were used to plot the electronic band structures, total DOSs, and PES. (http://www.gnuplot.info/ and https://inkscape.org/). Python scripts were used to generate data plots (https://www.python.org/). The relevant data has been reported in Tables 1−4 in the main manuscript. All the equilibrium structures with their crystallographic information files data involved in the subject reaction have been provided in the Supporting Information. The data for this study can be obtained at https://pubs.acs.org/.

### Supporting Information

The Supporting Information is available free of charge at https://pubs.acs.org/doi/10.1021/acsphyschemau.3c00035.

All the equilibrium structures involved in the subject reaction (PDF)



https://doi.org/10.1021/acsphyschemau.3c00035
ACS Phys. Chem Au 2024, 4, 40−56

## AUTHOR INFORMATION


### Corresponding Author

**Srimanta Pakhira** − *Theoretical Condensed Matter Physics and Advanced Computational Materials Science Laboratory, Department of Physics and Theoretical Condensed Matter Physics and Advanced Computational Materials Science Laboratory, Centre for Advanced Electronics (CAE), Indian Institute of Technology Indore (IIT Indore), Indore 453552 Madhya Pradesh, India;* orcid.org/0000-0002-2488-300X; Email: spakhira@iiti.ac.in, spakhirafsu@gmail.com

### Author

**Ashok Singh** − *Theoretical Condensed Matter Physics and Advanced Computational Materials Science Laboratory, Department of Physics, Indian Institute of Technology Indore (IIT Indore), Indore 453552 Madhya Pradesh, India*

Complete contact information is available at: https://pubs.acs.org/10.1021/acsphyschemau.3c00035


### Author Contributions

Dr. Pakhira developed the complete idea of this current research work, and Dr. Pakhira and Mr. Ashok Singh computationally studied the electronic structures and properties of the 2D monolayer Nb-$ZrSe_2$. Dr. Pakhira and Mr. Ashok Singh explored the whole reaction pathways, intermediates, and reaction barriers. Dr. Pakhira and Mr. Ashok Singh explained the ORR mechanism by the DFT calculations. Quantum calculations and theoretical models were designed and performed by Dr. Pakhira and Mr. Ashok Singh. Dr. Pakhira and Mr. Ashok Singh elucidated and analyzed the computed results and ORR mechanism. Dr. Pakhira and Mr. Ashok Singh wrote the whole manuscript and prepared all the tables and figures in the manuscript.

### Notes

The authors declare no competing financial interest.

## ACKNOWLEDGMENTS

We acknowledge the funding and technical support from the Science and Engineering Research Board-Department of Science and Technology (SERB-DST), Govt. of India under Grant No. CRG/2021/000572 and ECR/2018/000255. This research work is financially supported by the SERB-DST, Govt. of India under Grant No. CRG/2021/000572, ECR/2018/000255, and SB/S2/RJN-067/2017, SERB-DST, Govt. of India. Dr. Srimanta Pakhira acknowledges the Science and Engineering Research Board, Department of Science and Technology (SERB-DST), Government of India, for providing his highly prestigious Ramanujan Faculty Fellowship under the scheme no. SB/S2/RJN-067/2017, and for his Early Career Research Award (ECRA) under the grant No. ECR/2018/000255. Dr. Pakhira thanks to the SERB for providing the Core Research Grant (CRG), SERB-DST, Govt. of India under the scheme number CRG/2021/000572. Mr. Ashok Singh thanks University Grants Commission (UGC), Govt. of India for availing his doctoral fellowship under the ref. No: 1468/(CSIR-UGC NET JUNE 2019). The author would like to acknowledge the SERB-DST for providing the computing cluster and programs and IIT Indore for providing the basic infrastructure to conduct this research work. We thank the CSIR, Govt of India for providing the research funds under the scheme no. 22/0883/23/EMR-II. We recognize the support from the DST, Govt. of India for providing the FIST project to the Department of Physics, IIT Indore under the scheme number SR/FIST/PSI225/2016. We thank Indian Institute of Technology Indore (IIT Indore), MP, India for providing the basic infrastructure. We acknowledge the National Supercomputing Mission (NSM) for providing computing resources of 'PARAM Brahma' at IISER Pune, which is implemented by C-DAC and supported by the Ministry of Electronics and Information Technology (MeitY) and Department of Science and Technology (DST), Government of India.

## REFERENCES


(1) Chu, S.; Majumdar, A. Opportunities and Challenges for a Sustainable Energy Future. *Nature* **2012**, *488*, 294−303.

(2) Abdelkareem, M. A.; Elsaid, K.; Wilberforce, T.; Kamil, M.; Sayed, E. T.; Olabi, A. Environmental Aspects of Fuel Cells: A Review. *Sci. Total Environ.* **2021**, *752*, No. 141803.

(3) Chu, S.; Cui, Y.; Liu, N. The Path towards Sustainable Energy. *Nat. Mater.* **2017**, *16*, 16−22.

(4) Kartha, S.; Grimes, P. Fuel Cells: Energy Conversion for the Next Century. *Phys. Today* **1994**, *47*, 54−61.

(5) Gewirth, A. A.; Thorum, M. S. Electroreduction of Dioxygen for Fuel-Cell Applications: Materials and Challenges. *Inorg. Chem.* **2010**, *49*, 3557−3566.

(6) Duan, Z.; Wang, G. Comparison of Reaction Energetics for Oxygen Reduction Reactions on Pt(100), Pt(111), Pt/Ni(100), and Pt/Ni(111) Surfaces: A First-Principles Study. *J. Phys. Chem. C* **2013**, *117*, 6284−6292.

(7) Ying, J. Atomic-Scale Design of High-Performance Pt-Based Electrocatalysts for Oxygen Reduction Reaction. *Front. Chem.* **2021**, *9*, No. 753604.

(8) Kulkarni, A.; Siahrostami, S.; Patel, A.; Nørskov, J. K. Understanding Catalytic Activity Trends in the Oxygen Reduction Reaction. *Chem. Rev.* **2018**, *118*, 2302−2312.

(9) Nørskov, J. K.; Rossmeisl, J.; Logadottir, A.; Lindqvist, L.; Kitchin, J. R.; Bligaard, T.; Jónsson, H. Origin of the Overpotential for Oxygen Reduction at a Fuel-Cell Cathode. *J. Phys. Chem. B* **2004**, *108*, 17886−17892.

(10) Hung, A. J.; Yu, C. C.; Chen, Y. H.; Sung, L. Y. Cost Analysis of Proton Exchange Membrane Fuel Cell Systems. *AIChE J.* **2008**, *54*, 1798−1810.

(11) Othman, R.; Dicks, A. L.; Zhu, Z. Non Precious Metal Catalysts for the PEM Fuel Cell Cathode. *Int. J. Hydrogen Energy* **2012**, *37*, 357−372.

(12) Banham, D.; Ye, S.; Pei, K.; Ozaki, J. I.; Kishimoto, T.; Imashiro, Y. A Review of the Stability and Durability of Non-Precious Metal Catalysts for the Oxygen Reduction Reaction in Proton Exchange Membrane Fuel Cells. *J. Power Sources* **2015**, *285*, 334−348.

(13) Wang, B. Recent Development of Non-Platinum Catalysts for Oxygen Reduction Reaction. *J. Power Sources* **2005**, *152*, 1−15.

(14) Wang, Y.; Yang, Y.; Jia, S.; Wang, X.; Lyu, K.; Peng, Y.; Zheng, H.; Wei, X.; Ren, H.; Xiao, L.; Wang, J.; Muller, D. A.; Abruña, H. D.; Hwang, B. J.; Lu, J.; Zhuang, L. Synergistic Mn-Co Catalyst Outperforms Pt on High-Rate Oxygen Reduction for Alkaline Polymer Electrolyte Fuel Cells. *Nat. Commun.* **2019**, *10*, 6−13.

(15) Lu, X. F.; Chen, Y.; Wang, S.; Gao, S.; Lou, X. W. Interfacing Manganese Oxide and Cobalt in Porous Graphitic Carbon Polyhedrons Boosts Oxygen Electrocatalysis for Zn−Air Batteries. *Adv. Mater.* **2019**, *31*, No. 1902339.

(16) Lu, X. F.; Zhang, S. L.; Sim, W. L.; Gao, S.; Lou, X. W. Phosphorized $CoNi_2S_4$ Yolk-Shell Spheres for Highly Efficient Hydrogen Production via Water. *Angew. Chem., Int. Ed.* **2021**, *60*, 22885−22891.

(17) Liu, M.; Xiao, X.; Li, Q.; Luo, L.; Ding, M.; Zhang, B.; Li, Y.; Zou, J.; Jiang, B. Recent Progress of Electrocatalysts for Oxygen Reduction in Fuel Cells. *J. Colloid Interface Sci.* **2022**, *607*, 791−815.

(18) Li, F.; Xue, M. Two-Dimensional Transition Metal Dichalcogenides for Electrocatalytic Energy Conversion Applications.

In *Two-Dimensional Materials—Synthesis, Characterization and Potential Applications*, 1st ed.; Nayak, P. K., Eds.; IntechOpen: Rijeka, 2016; pp 64−84.
(19) Huang, H.; Feng, X.; Du, C.; Wu, S.; Song, W. Incorporated Oxygen in $MoS_2$ Ultrathin Nanosheets for Efficient ORR Catalysis. *J. Mater. Chem. A* **2015**, *3*, 16050−16056.
(20) Jaramillo, T. F.; Jørgensen, K. P.; Bonde, J.; Nielsen, J. H.; Horch, S.; Chorkendorff, I. Identification of Active Edge Sites for Electrochemical $H_2$ Evolution from $MoS_2$ Nanocatalysts. *Science* **2007**, *317*, 100−102.
(21) Yang, L.; Liu, P.; Li, J.; Xiang, B. Two-Dimensional Material Molybdenum Disulfides as Electrocatalysts for Hydrogen Evolution. *Catalysts* **2017**, *7*, 285.
(22) Chia, X.; Ambrosi, A.; Lazar, P.; Sofer, Z.; Pumera, M. Electrocatalysis of Layered Group 5 Metallic Transition Metal Dichalcogenides ($MX_2$, M = V, Nb, and Ta; X = S, Se, and Te). *J. Mater. Chem. A* **2016**, *4*, 14241−14253.
(23) Toh, R. J.; Sofer, Z.; Pumera, M. Catalytic Properties of Group 4 Transition Metal Dichalcogenides ($MX_2$; M = Ti, Zr, Hf; X = S, Se, Te). *J. Mater. Chem. A* **2016**, *4*, 18322−18334.
(24) Komsa, H. P.; Kotakoski, J.; Kurasch, S.; Lehtinen, O.; Kaiser, U.; Krasheninnikov, A. V. Two-Dimensional Transition Metal Dichalcogenides under Electron Irradiation: Defect Production and Doping. *Phys. Rev. Lett.* **2012**, *109*, No. 035503.
(25) Li, H.; Tsai, C.; Koh, A. L.; Cai, L.; Contryman, A. W.; Fragapane, A. H.; Zhao, J.; Han, H. S.; Manoharan, H. C.; Abild-Pedersen, F.; Nørskov, J. K.; Zheng, X. Erratum: Activating and Optimizing $MoS_2$ Basal Planes for Hydrogen Evolution through the Formation of Strained Sulphur Vacancies. *Nat. Mater.* **2016**, *15*, 364.
(26) Shi, Y.; Zhou, Y.; Yang, D.-R.; Xu, W.-X.; Wang, C.; Wang, F.-B.; Xu, J.-J.; Xia, X.-H.; Chen, H.-Y. Energy Level Engineering of $MoS_2$ by Transition-Metal Doping for Accelerating Hydrogen Evolution Reaction. *J. Am. Chem. Soc.* **2017**, *139*, 15479−15485.
(27) Upadhyay, S. N.; Pakhira, S. Mechanism of Electrochemical Oxygen Reduction Reaction at Two-Dimensional Pt-Doped $MoSe_2$ material: An Efficient Electrocatalyst. *J. Mater. Chem. C* **2021**, *9*, 11331−11342.
(28) You, B.; Tang, M. T.; Tsai, C.; Abild-Pedersen, F.; Zheng, X.; Li, H. Enhancing Electrocatalytic Water Splitting by Strain Engineering. *Adv. Mater.* **2019**, *31*, No. 1807001.
(29) Jin, H.; Guo, C.; Liu, X.; Liu, J.; Vasileff, A.; Jiao, Y.; Zheng, Y.; Qiao, S. Z. Emerging Two-Dimensional Nanomaterials for Electrocatalysis. *Chem. Rev.* **2018**, *118*, 6337−6408.
(30) Xiao, B. B.; Zhang, P.; Han, L. P.; Wen, Z. Functional $MoS_2$ by the Co/Ni Doping as the Catalyst for Oxygen Reduction Reaction. *Appl. Surf. Sci.* **2015**, *354*, 221−228.
(31) Urbanová, V.; Lazar, P.; Antonatos, N.; Sofer, Z.; Otyepka, M.; Pumera, M. Positive and Negative Effects of Dopants toward Electrocatalytic Activity of $MoS_2$ and $WS_2$: Experiments and Theory. *ACS Appl. Mater. Interfaces* **2020**, *12*, 20383−20392.
(32) Huang, H.; Feng, X.; Du, C.; Song, W. High-Quality Phosphorus-Doped $MoS_2$ Ultrathin Nanosheets with Amenable ORR Catalytic Activity. *Chem. Commun.* **2015**, *51*, 7903−7906.
(33) Singh, Y.; Back, S.; Jung, Y. Activating Transition Metal Dichalcogenides by Substitutional Nitrogen-Doping for Potential ORR Electrocatalysts. *ChemElectroChem.* **2018**, *5*, 4029−4035.
(34) Tian, S.; Tang, Q. Activating Transition Metal Dichalcogenide Monolayers as Efficient Electrocatalysts for the Oxygen Reduction Reaction via Single Atom Doping. *J. Mater. Chem. C* **2021**, *9*, 6040−6050.
(35) Zhang, M.; Zhu, Y.; Wang, X.; Feng, Q.; Qiao, S.; Wen, W.; Chen, Y.; Cui, M.; Zhang, J.; Cai, C.; Xie, L. Controlled Synthesis of $ZrS_2$ Monolayer and Few Layers on Hexagonal Boron Nitride. *J. Am. Chem. Soc.* **2015**, *137*, 7051−7054.
(36) Mahamudujjaman, M.; Afzal, M. A.; Islam, R. S.; Naqib, S. H. First-Principles Insights into Mechanical, Optoelectronic, and Thermo-Physical Properties of Transition Metal Dichalcogenides $ZrX_2$ (X = S, Se, and Te). *AIP Adv.* **2022**, *12*, No. 025011.
(37) Gong, C.; Zhang, H.; Wang, W.; Colombo, L.; Wallace, R. M.; Cho, K. Band Alignment of Two-Dimensional Transition Metal Dichalcogenides: Application in Tunnel Field Effect Transistors. *Appl. Phys. Lett.* **2013**, *103*, No. 053513.
(38) Lee, J.; Kang, S.; Yim, K.; Kim, K. Y.; Jang, H. W.; Kang, Y.; Han, S. Hydrogen Evolution Reaction at Anion Vacancy of Two-Dimensional Transition-Metal Dichalcogenides: Ab Initio Computational Screening. *J. Phys. Chem. Lett.* **2018**, *9*, 2049−2055.
(39) Som, N. N.; Jha, P. K. Hydrogen Evolution Reaction of Metal Di-Chalcogenides: $ZrS_2$, $ZrSe_2$ and Janus ZrSSe. *Int. J. Hydrogen Energy* **2020**, *45*, 23920−23927.
(40) Mañas-Valero, S.; García-López, V.; Cantarero, A.; Galbiati, M. Raman Spectra of $ZrS_2$ and $ZrSe_2$ from Bulk to Atomically Thin Layers. *Appl. Sci.* **2016**, *6*, 264.
(41) Felseghi, R. A.; Carcadea, E.; Raboaca, M. S.; Trufin, C. N.; Filote, C. Hydrogen Fuel Cell Technology for the Sustainable Future of Stationary Applications. *Energies* **2019**, *12*, 4593.
(42) Maheshwari, K.; Sharma, S.; Sharma, A.; Verma, S. Fuel Cell and Its Applications: A Review. *Int. J. Eng. Res. Technol.* **2018**, *7*, 6−9.
(43) Dange, P.; Savla, N.; Pandit, S.; Bobba, R.; Jung, S. P.; Gupta, P. K.; Sahni, M.; Prasad, R. A Comprehensive Review on Oxygen Reduction Reaction in Microbial Fuel Cells. *J. Renew. Mater.* **2022**, *10*, 665−697.
(44) Marković, N. M.; Schmidt, T. J.; Stamenković, V.; Ross, P. N. Oxygen Reduction Reaction on Pt and Pt Bimetallic Surfaces: A Selective Review. *Fuel Cells* **2001**, *1*, 105−116.
(45) Nie, Y.; Li, L.; Wei, Z. Recent Advancements in Pt and Pt-Free Catalysts for Oxygen Reduction Reaction. *Chem. Soc. Rev.* **2015**, *44*, 2168−2201.
(46) Hui, J.; Pakhira, S.; Bhargava, R.; Barton, Z. J.; Zhou, X.; Chinderle, A. J.; Mendoza-Cortes, J. L.; Rodríguez-López, J. Modulating Electrocatalysis on Graphene Heterostructures: Physically Impermeable Yet Electronically Transparent Electrodes. *ACS Nano* **2018**, *12*, 2980−2990.
(47) Duan, Z.; Wang, G. A First Principles Study of Oxygen Reduction Reaction on a Pt (111) Surface Modified by a Subsurface Transition Metal M (M = Ni, Co, or Fe). *Phys. Chem. Chem. Phys.* **2011**, *13*, 20178−20187.
(48) Fazio, G.; Ferrighi, L.; Perilli, D.; Di Valentin, C. Computational Electrochemistry of Doped Graphene as Electrocatalytic Material in Fuel Cells. *Int. J. Quantum Chem.* **2016**, *116*, 1623−1640.
(49) Kan, D.; Wang, D.; Zhang, X.; Lian, R.; Xu, J.; Chen, G.; Wei, Y. Rational Design of Bifunctional ORR/OER Catalysts Based on Pt/Pd-Doped $Nb_2CT_2$ MXene by First-Principles Calculations. *J. Mater. Chem. A* **2020**, *8*, 3097−3108.
(50) Ji, Y.; Yang, M.; Dong, H.; Wang, L.; Hou, T.; Li, Y. Monolayer Group IVA Monochalcogenides as Potential and Efficient Catalysts for the Oxygen Reduction Reaction from First-Principles Calculations. *J. Mater. Chem. A* **2017**, *5*, 1734−1741.
(51) Hu, R.; Li, Y.; Zeng, Q.; Shang, J. Applied Surface Science Role of Active Sites in N-Coordinated Fe-Co Dual-Metal Doped Graphene for Oxygen Reduction and Evolution Reactions : A Theoretical Insight. *Appl. Surf. Sci.* **2020**, *525*, No. 146588.
(52) Dovesi, R.; Erba, A.; Orlando, R.; Zicovich-Wilson, C. M.; Civalleri, B.; Maschio, L.; Rérat, M.; Casassa, S.; Baima, J.; Salustro, S.; Kirtman, B. Quantum-Mechanical Condensed Matter Simulations with CRYSTAL. *Wiley Interdiscip. Rev. Comput. Mol. Sci.* **2018**, *8*, No. e1360.
(53) Grimme, S.; Antony, J.; Ehrlich, S.; Krieg, H. A Consistent and Accurate Ab Initio Parametrization of Density Functional Dispersion Correction (DFT-D) for the 94 Elements H-Pu. *J. Chem. Phys.* **2010**, *132*, No. 154104.
(54) Chen, Z.-y.; Yang, J.-l. The B3LYP Hybrid Density Functional Study on Solids. *Front. Phys. China* **2006**, *1*, 339−343.
(55) Muscat, J.; Wander, A.; Harrison, N. M. On the Prediction of Band Gaps from Hybrid Functional Theory. *Chem. Phys. Lett.* **2001**, *342*, 397−401.
(56) Tosoni, S.; Tuma, C.; Sauer, J.; Civalleri, B.; Ugliengo, P. A Comparison Between Plane Wave and Gaussian-Type Orbital Basis

Sets for Hydrogen Bonded Systems: Formic Acid as a Test Case. *J. Chem. Phys.* **2007**, *127*, No. 154102.
(57) Adhikari, K.; Chakrabarty, A.; Bouhali, O.; Mousseau, N.; Becquart, C. S.; El-Mellouhi, F. Benchmarking the Performance of Plane-Wave vs. Localized Orbital Basis Set Methods in DFT Modeling of Metal Surface: A Case Study for Fe-(110). *J. Comput. Sci.* **2018**, *29*, 163−167.
(58) Dovesi, R.; Pascale, F.; Civalleri, B.; Doll, K.; Harrison, N. M.; Bush, I.; D'Arco, P.; Noel, Y.; Rerat, M.; Carbonniere, P.; Causa, M.; Salustro, S.; Lacivita, V.; Kirtman, B.; Ferrari, A. M.; Gentile, F. S.; Baima, J.; Ferrero, M.; Demichelis, R.; De La Pierre, M. The CRYSTAL Code, 1976−2020 and Beyond, a Long Story. *J. Chem. Phys.* **2020**, *152*, No. 204111.
(59) Paier, J.; Diaconu, C. V.; Scuseria, G. E.; Guidon, M.; Vandevondele, J.; Hutter, J. Accurate Hartree-Fock Energy of Extended Systems Using Large Gaussian Basis Sets. *Phys. Rev. B* **2009**, *80*, No. 174114.
(60) Vilela Oliveira, D.; Laun, J.; Peintinger, M. F.; Bredow, T. BSSE-Correction Scheme for Consistent Gaussian Basis Sets of Double- and Triple-Zeta Valence with Polarization Quality for Solid-State Calculations. *J. Comput. Chem.* **2019**, *40*, 2364−2376.
(61) Laun, J.; Vilela Oliveira, D.; Bredow, T. Consistent Gaussian Basis Sets of Double- and Triple-Zeta Valence with Polarization Quality of the Fifth Period for Solid-State Calculations. *J. Comput. Chem.* **2018**, *39*, 1285−1290.
(62) Singh, A.; Pakhira, S. Unraveling the Electrocatalytic Activity of Platinum Doped Zirconium Disulfide toward the Oxygen Reduction Reaction. *Energy Fuels* **2023**, *37*, 567−579.
(63) Bocharov, D.; Piskunov, S.; Zhukovskii, Y. F.; Evarestov, R. A. Ab Initio Calculations on the Electronic Structure and Photocatalytic Properties of Two-Dimensional $WS_2$ (0001) Nanolayers of Varying Thickness. *Phys. Status Solidi - Rapid Res. Lett.* **2019**, *13*, No. 1800253.
(64) Piskunov, S.; Lisovski, O.; Zhukovskii, Y. F.; D'yachkov, P. N.; Evarestov, R. A.; Kenmoe, S.; Spohr, E. First-Principles Evaluation of the Morphology of $WS_2$ Nanotubes for Application as Visible-Light-Driven Water-Splitting Photocatalysts. *ACS Omega* **2019**, *4*, 1434−1442.
(65) Fukuda, Y.; Sasanuma, Y. Computational Characterization of Nylon 4, a Biobased and Biodegradable Polyamide Superior to Nylon 6. *ACS Omega* **2018**, *3*, 9544−9555.
(66) Hojamberdiev, M.; Bekheet, M. F.; Hart, J. N.; Vequizo, J. J. M.; Yamakata, A.; Yubuta, K.; Gurlo, A.; et al. Elucidating the Impact of A-Site Cation Change on Photocatalytic $H_2$ and $O_2$ Evolution Activities of Perovskite-Type $LnTaON_2$ (Ln = La and Pr). *Phys. Chem. Chem. Phys.* **2017**, *19*, 22210−22220.
(67) Monkhorst, H. J.; Pack, J. D. Special Points for Brillouin-Zone Integrations. *Phys. Rev. B* **1976**, *13*, 5188−5192.
(68) Momma, K.; Izumi, F. VESTA 3 for Three-Dimensional Visualization of Crystal, Volumetric and Morphology Data. *J. Appl. Crystallogr.* **2011**, *44*, 1272−1276.
(69) Upadhyay, S. N.; Sardar, V. B.; Singh, A.; Kumar, V.; Pakhira, S. Elucidating the Oxygen Reduction Reaction Mechanism on the Surfaces of 2D Monolayer $CsPbBr_3$ Perovskite. *Phys. Chem. Chem. Phys.* **2022**, *24*, 28283−28294.
(70) Upadhyay, S. N.; Pakhira, S. Nanostructured Pt-Doped 2D $MoSe_2$: An Efficient Bifunctional Electrocatalyst for Both Hydrogen Evolution and Oxygen Reduction Reactions. *Phys. Chem. Chem. Phys.* **2022**, *24*, 22823−22844.
(71) Sun, H.; Li, J.; Almheiri, S.; Xiao, J. Oxygen Reduction on a Pt (111) Catalyst in HT-PEM Fuel Cells by Density Functional Theory. *AIP Adv.* **2017**, *7*, No. 085020.
(72) Chretien, S.; Metiu, H. $O_2$ Evolution on a Clean Partially Reduced Rutile $TiO_2$ (110) Surface and on the Same Surface Precovered with $Au_1$ and $Au_2$: The Importance of Spin Conservation. *J. Chem. Phys.* **2008**, *129*, No. 074705.
(73) Snyder, J. W.; Skovsen, E.; Lambert, J. D. C.; Ogilby, P. R. Subcellular, Time-Resolved Studies of Singlet Oxygen in Single Cells. *J. Am. Chem. Soc.* **2005**, *127*, 14558−14559.
(74) Schweitzer, C.; Schmidt, R. Physical Mechanisms of Generation and Deactivation of Singlet Oxygen. *Chem. Rev.* **2003**, *103*, 1685−1757.
(75) Mtangi, W.; Kiran, V.; Fontanesi, C.; Naaman, R. Role of the Electron Spin Polarization in Water Splitting. *J. Phys. Chem. Lett.* **2015**, *6*, 4916−4922.
(76) Zhou, Y.; Gao, G.; Kang, J.; Chu, W.; Wang, L. Transition Metal-Embedded Two-Dimensional $C_3N$ as a Highly Active Electrocatalyst for Oxygen Evolution and Reduction Reactions. *J. Mater. Chem. A* **2019**, *7*, 12050−12059.
(77) Ji, J.; Zhang, C.; Qin, S.; Jin, P. Covalent − Organic Framework Electrocatalysts for Oxygen Evolution/Reduction and Hydrogen. *Sustain. Energy Fuels* **2021**, *5*, 5615−5626.
(78) Lu, S.; Zhang, Y.; Lou, F.; Guo, K.; Yu, Z. Applied Surface Science Non-Precious Metal Activated $MoSi_2N_4$ Monolayers for High-Performance OER and ORR Electrocatalysts : A First-Principles Study. *Appl. Surf. Sci.* **2022**, *579*, No. 152234.
(79) Xiao, B.; Zhu, H.; Liu, H.; Jiang, X.; Jiang, Q. The Activity Improvement of the Monolayer for Oxygen Reduction Electrocatalysis : A Density Functional Theory Study. *Front Chem.* **2018**, *6*, 351.
(80) Iyemperumal, S. K.; Deskins, N. A. Evaluating Solvent Effects at the Aqueous/Pt(111) Interface. *ChemPhysChem* **2017**, *18*, 2171−2190.
(81) Carrasco, J.; Hodgson, A.; Michaelides, A. A Molecular Perspective of Water at Metal Interfaces. *Nat. Mater.* **2012**, *11*, 667−674.
(82) Wang, Y.; Li, Y.; Heine, T. PtTe Monolayer: Two-Dimensional Electrocatalyst with High Basal Plane Activity toward Oxygen Reduction Reaction. *J. Am. Chem. Soc.* **2018**, *140*, 12732−12735.


https://doi.org/10.1021/acsphyschemau.3c00035
*ACS Phys. Chem Au* 2024, 4, 40−56